NASA TECHNICAL MEMORANDUM

NASA TM X-71424

NASA TM X-71424

SPUTTER EROSION AND DEPOSITION IN THE DISCHARGE CHAMBER OF A SMALL MERCURY ION THRUSTER

by John L. Power
Lewis Research Center
Cleveland, Ohio 44135

TECHNICAL PAPER proposed for presentation at
Tenth Electric Propulsion Conference sponsored
by the American Institute of Aeronautics and Astronautics
Lake Tahoe, Nevada, October 31-November 2, 1973

SPUTTER EROSION AND DEPOSITION IN THE DISCHARGE CHAMBER OF A SMALL MERCURY ION THRUSTER

John L. Power
Lewis Research Center
National Aeronautics and Space Administration
Cleveland, Ohio

Abstract

A 5-cm diameter mercury ion thruster similar to one tested for 9715 hours was operated ~400 hrs each at discharge voltages of 36.6, 39.6, and 42.6 V, with corresponding discharge propellant utilizations of 58, 68, and 70 percent. The observed sputter erosion rates of the internal thruster parts and the anode weight gain rate all rose rapidly with discharge voltage and were roughly in the ratio of 1:3:5 for the three voltages. The combined weight loss of the internal thruster parts nearly balanced the anode weight gain. Hg^{+2} ions apparently caused most of the observed erosion.

I. Introduction

A 5-cm diameter electron bombardment mercury ion thruster has been developed by the Hughes Research Laboratories, under NASA contract,[1, 2] for station-keeping and attitude control of satellites in synchronous Earth orbit. Use of mercury ion thrusters for such applications requires reliable thruster operation for thousands of hours, perhaps as high as 20,000 hours.[3] In addition to operating for long durations, many auxiliary propulsion applications require a beam vectoring capability, such as the electrostatic vector grid system developed by Hughes.[2, 4]

A 5-cm mercury ion thruster, the Hughes SIT-5 has recently been endurance tested at the NASA-Lewis Research Center for a total of 9715 hours. As reported by Nakanishi and Finke,[5] this life test was terminated because several of the accelerator grid members had been severed by localized direct impingement of badly defocused ion beamlets emerging from the screen grid. This defocusing was caused by metallic flakes which had fallen due to gravity onto the upstream side of the screen grid, partially blocking the affected grid holes.

The metallic flakes responsible for the ion defocusing in the endurance test were identified as sputtered material, which had deposited on the interior surface of the discharge chamber anode. This material ultimately peeled from the upstream portion of the anode and dropped onto the screen grid.

The investigation here reported was undertaken in an effort to determine the origin and composition of the anode sputter deposits seen in the endurance test, measure the sputter erosion rates of the internal discharge chamber parts and the deposition rate of the sputtered material on the anode, and identify, if possible, the species mainly responsible for the sputtering. In the expectation that the sputter erosion and deposition rates would strongly depend on the discharge potential ΔV_I, long term tests were planned at three values of ΔV_I within the acceptable ΔV_I range for mercury thruster operation. It was hoped that the results of these tests would indicate ways to greatly reduce or eliminate sputter erosion and deposition in the discharge chamber.

II. Experimental

Apparatus

A 5-cm mercury ion thruster, SIT-5, essentially identical to that employed in the aforementioned 9715-hour endurance test, was utilized in the tests here reported. A sectional drawing of the thruster discharge chamber, drawn to scale and showing all the component parts and materials, is presented in Figure 1.

The thruster was equipped with an advanced design Hughes electrostatic vector grid system,[2] shown in Figure 2 from the accelerator side. This grid system, which permits the thruster beam to be electrostatically vectored up to 10° in any direction, employs a screen grid with graded hole diameters. Views of the screen grid, with and without the anode pole piece insert installed, are shown in Figures 3(a) and (b). The screen grid and all the other discharge chamber components and surfaces except for the anode and the cathode keeper are always at cathode potential.

Both the main and the neutralizer cathodes were nearly identical to the standard Hughes designs,[6] and both were equipped with rolled tantalum foil inserts. The main cathode was part of an integrated cathode-isolator-vaporizer assembly.[1] The neutralizer was aimed directly downstream parallel to the thruster axis.

The thruster was always operated with the mercury feed reservoirs maintained at neutralizer common potential, hence with the net accelerating potential (minus ΔV_I) aways applied across the isolator. To remedy a previously observed problem, a temporary shield was fabricated and installed around the isolator in order to protect its external surface from collecting deposits during operation. The isolator was found to operate throughout the tests without measurable leakage current.

The power processing and control package used to operate the thruster is described by Hudson and Banks.[3] It incorporates a feedback control loop which acts by changing the power supplied to the main cathode vaporizer proportionately to the difference between the sensed ΔV_I in the discharge chamber and an adjustable control setting. This permits the ΔV_I to be maintained at any desired value within the operating range during long term unattended operation. J_E is independently controllable and may be set and adjusted to achieve extraction of the desired constant beam current J_B from the thruster. Since in these tests the ΔV_I was the principal independent variable, the above-described control loop was essential for continuous, generally unattended thruster operation at different constant values of ΔV_I and a fixed standard value of J_B. However, the automatic functioning of the control loop does cause continual small changes in the main cathode mercury flow.

In order to keep the thruster running at the set ΔV_I, the neutralizer was operated open loop

during the tests, the power to the neutralizer vaporizer being set and manually adjusted to maintain the desired standard mercury flow rate. The keeper discharges of both the main and the neutralizer cathodes were current-controlled and maintained at standard keeper current values.

Because of the importance of ΔV_I in these tests, this voltage was directly measured to an accuracy of better than ±0.1 V by an electrically floating, digital voltmeter. The other electrical parameters were measured by panel meters or by digital readout of analog signals. In addition, the important thruster variables were automatically recorded on chart paper by a multipoint recorder once a minute throughout the tests.

The experiments were conducted in a 4.88-m long by 1.52-m diameter vacuum tank with the thruster mounted in a 0.90-m diameter port at one end of the facility. The thruster beam was axially directed into the tank at a metal target located in the middle of the tank. The normal facility pressure was approximately 1×10^{-6} torr.

A movable beam current probe was briefly utilized during the tests to take the data for a current density profile of the thruster beam. The probe, which consists of eleven Faraday cup detectors located 1.27-cm apart in a straight line, can be moved perpendicularly across the thruster beam in a plane normal to the beam axis. The distance between the plane of the probe face and that of the downstream edges of the accelerator grid members was 12.1 cm. Current readings were always made with a 10-V negative bias applied to the probe in order to prevent any electron collection. The measured currents were taken to be directly proportional to the beam current density at each detector hole location.

Test Conditions and Operation

Prior to the start of these tests the thruster had been operated for approximately 600 hours in various performance tests, utilizing the same components and configuration. The initial condition of all the thruster components was well documented before the present investigation was begun.

The three extended thruster tests conducted in this work were done at constant values of ΔV_I = 39.6, 36.6, and 42.6 V and were carried out in that order. During each test the main discharge was maintained for 416 hours and the beam and accelerator voltages were on for 400 to 409 hours, the specific times being given in Table I.

Typical values of several important operating parameters during the tests are given in Table I. For the 39.6 V ΔV_I test, these values are the same as the values established for the Hughes 5-cm thruster.[2] For the 36.6 and 42.6 V ΔV_I tests, the operating parameter values shown in Table I were dictated by the thruster operating characteristics, constant ΔV_I requirements, and 23.4 mA J_B. Ranges about the set points within which ΔV_I, J_B, and J_E remained at least 99 percent of the time during each test were about ±0.6 V, ±0.8 mA, and ±8 mA, respectively.

Early in the first test conducted, with ΔV_I = 39.6 V, beam profile measurements were made using the beam probe apparatus previously described. The beam probe was exposed to intense ion bombardment from the beam for about $3\frac{1}{2}$ hours during these measurements, resulting in substantial back sputtering of stainless steel from its surface toward the ion thruster. On examination of the ion thruster shortly after the measurements were made, a definite stainless steel sputter coating was evident on the accelerator grid system, but no sputtered material from the beam probe was observed on the internal discharge chamber parts and surfaces. After further thruster operation, however, it was found that all of the sputtered stainless steel coating on the grid surfaces had been sputtered away. The assumption has been made that the sputtered stainless steel coating could be neglected in the weight changes determined for this ΔV_I test.

Analytical Procedures

Prior to the initial test and following each of the three tests in this work, the ion thruster discharge chamber was disassembled and all of its major component parts carefully observed, weighed, measured, and photographed in order to document the changes caused by the tests. Neither the thruster body-anode assembly nor the electrostatic vector grid system, however, could be readily dismantled without the danger of significant alteration on reassembly, so these assemblies were examined intact.

The weights of the discharge chamber parts were obtained both with a single pan, high capacity balance reading to 1 mg and with an analytical balance reading to 0.01 mg and having a capacity of 100 g. With the latter, weighings reproducible to <0.05 mg could be and were made. With the high capacity balance, weighings reproducible to 1 mg could easily be made. The weight changes of the parts due to erosion in the tests, as determined with both balances, were always in agreement within the reproducibility of the high capacity balance. The thruster component weight changes determined with the analytical balance and quoted in the Results section to 0.01 mg are estimated to have possible errors of ±0.10 mg due to weighing inaccuracies. The grid assembly weight changes, which could only be determined with the high capacity balance and which are therefore given only to 1 mg in the Results section, are estimated to have possible weighing errors of ±2 mg. For most of the thruster components additional uncertainties could exist in the measured weight changes due to several other factors than the weighing inaccuracies. These factors include such things as weight changes during the assembly and disassembly of the parts themselves. However, the consistency of the weight changes found suggests that the errors introduced by all these sources were small compared with the weight changes determined.

Standard arc emission spectrographic analyses were performed on several samples of sputter-deposited material, coatings, and loose flakes obtained from the ΔV_I tests here reported and from the 5-cm thruster used in the 9715-hour endurance test. In these analyses the metallic samples were first dissolved in acid, then the solutions were analyzed for their elemental composition by arc excitation. The standard deviation errors quoted in the analyses are ±10 percent of the amount determined for each detected element, except that for

trace constituents the errors rise as the normal detection limit of 0.01 to 0.1 weight percent is approached.

Scanning electron microscope (SEM) examinations were performed on several sputter-coated pieces of the thruster anode following completion of all the ΔV_I tests. Like examinations were also made of sputter-coated sections of the anode from the endurance-tested five cm thruster and on individual sputter-deposited flakes from this anode.

Such SEM examinations provide data on the smoothness, texture or grain size, thickness, and uniformity of the coating surfaces. Edge examination also discloses any layered structure in the sputtered coatings. Furthermore, SEM studies of the substrate under or near the edge of a partially peeled coating flake can reveal how cleanly the flake has separated from the substrate surface.

The SEM used has a useful magnification range of 50 to 10,000 times. Its electron beam energy was held fixed at 25 keV.

The fluorescent X-ray detection and analysis system built into the SEM was used to provide elemental identification and other analytical information. The X-rays detected and analyzed are essentially emitted only from the viewed surface, typically 1 to 2 μm. Hence small surface regions or inhomogeneities may be analyzed. The sputter coatings examined were at all times greater than the electron beam penetration; the X-ray analyses conducted on them were without interference from the coating substrate material.

The detected strength of a given X-ray emitted by an element of interest, relative to that of an X-ray from an arbitrary standard element, may be taken to be approximately proportional to the concentration ratio of the two elements in the surface layer being analyzed. This relationship permits semiquantitative analytical information to be extracted from the X-ray analyses. In the present work, iron was found to be a substantial constituent in nearly all the coatings, flakes, and substrates analyzed; hence it was generally taken as the standard element. The strongest iron X-ray, the K_α X-ray at 6.4 keV was thus taken as the standard peak in calculating these peak strength ratios. The X-ray peak strengths themselves were measured by the respective peak height above the background distribution.

III. Results

Weight Changes and Observations

The eight discharge chamber components which were individually weighed, measured, and examined before and after each of the three ΔV_I tests in this investigation were: the cathode assembly shield, the cathode pole piece assembly (including the baffle screw), the baffle, the baffle holddown nut, the thruster backplate, the thruster body-anode assembly, the anode pole piece insert, and the vector grid assembly. See Figure 1 for the location of each of these in the assembled thruster. The initial weights, the weight changes for each test, and the average weight change rates during each test are listed in Table II as determined for each of the eight components. The only measured dimension which changed sufficiently during the tests so that accurate values of the dimensioned change could be obtained was the tip diameter of the baffle screw (measured ~0.8 mm from the actual end of the screw). Values determined for the change and change rate in this dimension during the three tests are also included in Table II.

It will be noted from Table II that all the thruster components were eroded and lost weight in all the tests except for the thruster body-anode assembly, which gained weight in each of the tests. In Figure 4 the weight loss or gain rates from Table II are semilogarithmically plotted versus the nominal ΔV_I for each test. Ratios of the weight loss or gain rates for each component during the three tests are compiled in Table III, together with the component construction material or materials. The sharp rise with increasing ΔV_I found in the erosion or weight gain rates of all the thruster components except the vector grid assembly and thruster backplate is evident from Figure 4 and Table III.

Careful observations of each of the discharge chamber components before and after each of the three ΔV_I tests revealed no erosion or deposition process peculiar to any one specific test. Evidences of erosion and deposition were observed in all three tests.

The cathode assembly shield, made of tantalum, is shown after the second test in Figure 5, as viewed from the downstream side. It showed hardly any discernible change throughout the tests. Its thickness at the inside diameter, which is closest to the discharge emerging from the cathode, did not change during the tests within the measuring uncertainty

A downstream view of the disassembled cathode pole piece is shown in Figure 6(c) and side views of the pole piece with the baffle and the baffle holddown nut assembled on the baffle screw are shown in Figures 6(a) and (b). The screw is integral to the pole piece. The pole piece is of type 1010 mild steel, the screen is tantalum, and the baffle screw and its support wires are 302 stainless steel.

In Figure 6, view (a) was taken before the start of the first test, views (b) and (c) following the conclusion of the third test. The bulk of the erosion of the exposed screw diameter occurred during the final test (with ΔV_I = 42.6 V). The measured decrease in this diameter is documented in Table II. Note the uniformity of the eroded screw diameter in Figure 6(b). The screw length decreased slightly (~0.3 mm) during the tests and some chamfering of the screw tip to a more pointed shape also took place.

Erosion of both the inner and the outer downstream-facing surfaces of the cathode pole piece was observed, but no erosion of the tantalum screen was evident. Measurements of the outer edge thickness of the pole piece were taken only for the final test, during which this thickness decreased ~0.008 mm. Interestingly, the outer downstream edge of the pole piece was not significantly rounded or chamfered despite the erosion of the adjacent surface.

A side view of the baffle and holddown nut following the final test is shown in Figure 7, with their downstream faces up. The 0.635-cm diameter tantalum baffle lost little weight even though its exposed downstream surface plainly showed some erosion. The edge thickness of the baffle and its outside diameter were reduced by ~0.010 mm as a result of the three tests. No rounding or chamfering of the outer baffle edges was observed, nor was any evidence of erosion seen on the upstream side of the baffle.

The baffle holddown nut, made of type 302 stainless steel, did show substantial erosion. As is evident by comparing Figure 6(a) with Figure 7, the downstream outside diameter of the nut was particularly reduced, as was the thickness of the nut (measured between the flat surfaces near the outside diameter) decreasing 0.053 mm. Decreases were noted as well across the nut corners and flats (on the upstream side), amounting to 0.081 mm and 0.015 mm, respectively.

Figure 8 shows the downstream side of the thruster backplate following the first test (at ΔV_I = 39.6 V). The appearance of the type 1010 mild steel backplate, was very similar to this after each test. The annular region exposed to the thruster discharge is evident by the erosion pattern. Measurements of the backplate thickness near the middle of the eroded region indicated a decrease of about 0.015 mm in the plate thickness. The uneroded circular central region of the backplate is covered by the cathode pole piece. Immediately surrounding this region is an annular area, approximately 0.32-cm wide, which quite clearly is more heavily eroded than the rest of the backplate. The screw holes in this region accommodate four screws which attach the cathode-isolator-vaporizer assembly to the backplate. Throughout the tests the ends of these screws extended from 0.54 to 1.57 mm into the discharge chamber. Each screw hole itself had a narrow annular region of heavier erosion around it, caused by the screws extending beyond the surface.

The thruster body-anode assembly (304 stainless steel) is shown in Figure 9(a) as viewed looking downstream. The photograph was taken following the final test. This assembly was the only discharge chamber component to gain weight during the tests (see Table II). The weight gain clearly was due to a coating of sputtered material on the interior of the anode. Figure 9(b) shows an upstream portion of the coated anode following the final test, with the engine body in the background. The anode coating always displayed the very dull, uniform mat gray appearance which can be indistinctly seen in the figure. No inhomogeneities or flakes were visible even across the anode stiffening indentations or at the tightly folded-over upstream end.

On disassembly of the anode following the final test, a thin coating of sputtered material having the same appearance as the anode coating was found over all of the anode exterior and thruster body interior surface area except for a circumferential band near the middle of each of these surfaces. These uncoated bands were both ~2.2-cm wide and coincided in their location.

Both end regions of the thruster body interior surface, not covered by the anode, developed shiny, irregular, lumpy deposits of sputtered material, Figure 9(b). Samples were collected from both ends of the thruster body interior surface. Small amounts of loose metallic chips were also found on the thruster body interior following both the first test at ΔV_I = 39.6 V and the final test at ΔV_I = 42.6 V. These closely resembled in appearance the scraped-off deposits described above. Figure 10 shows a magnified view of some of the approximately 0.5 mg of chips collected, ranging in size from <0.025 mm to >0.50 mm across.

The anode pole piece insert (type 1010 mild steel plated with nickel) showed little erosion damage although it had a splotchy, tarnished appearance on both its upstream and downstream surfaces (Fig. 11) throughout the tests. The erosion did not penetrate the nickel plating, and no substrate iron corrosion was ever observed on the insert.

The vector grid assembly (Figs. 2 and 3(b)) combines the screen grid and the accelerator grid system. All parts of the assembly exposed to either the thruster discharge or beam are of high purity molybdenum. Erosion of all these parts was evident after each test.

Figure 3(a) shows the discharge chamber side of the screen grid before the start of the first test, while Figure 3(b) shows the same surface following the final test. This surface displayed nearly identical erosion features after each of the three tests. The most noticeable is the decrease in graininess and apparent erosion severity with increasing radius. Heavily eroded, shadow-like regions extend radially outward from the sixteen outermost grid holes. A final feature is the raised, concave, ~1.5-mm wide bank extending around the grid from inside its exposed perimeter to the exposed perimeter of the grid. The bank indicated that the entire grid area inside it had been eroded away to a significant depth (perhaps 0.1 mm). Examination of the downstream side of the screen grid revealed no significant erosion or significant deposition.

Normal charge exchange and direct ion impingement erosion of the accelerator grid elements was observed. Many examples of both types of erosion may be seen in Figure 2, which shows the accelerator grid system after the final test, and in Figures 12(a) and (b), which show the portion of the accelerator grid system nearest the neutralizer before the first test and after the final test. The direct ion impingement erosion did not change over the course of the tests. This erosion was particularly evident at the outermost grid apertures, and was concentrated on the charge exchange pads, adjacent to the central grid apertures, and appeared as depressions and grooves on these pads. It was particularly extensive during the ΔV_I = 36.6 V test, correlating with the increased mercury flow rate and much reduced discharge chamber propellant utilization during this test.

Analytical Results and Electron Microscope Studies

The results from the emission spectrographic analyses performed in this investigation are compiled in Table IV. All the results are given in terms of weight percent of the listed metal in the total metallic content of the sample.

The analyzed samples are divided into four groups. The first of these comprises three samples of the coating of sputtered material on the interior of the anode after completion of all the ΔV_I tests. These samples were removed from downstream, middle, and upstream locations on a lengthwise strip of the anode by flexing each portion of the strip until a sufficient amount of the coating to analyze had spalled or broken off from the desired location.

The second group were all collected from the interior of the thruster body after the final ΔV_I test. The first and third of these were scraped from the downstream and upstream ends of the body while the second consisted of the metal chips shown in Figure 10, which were collected from the body on disassembly of the thruster.

The three samples in the third group came from the 9715-hr 5-cm thruster following termination of that test. Two of these samples consisted of flakes found resting on the upstream surface of the screen grid. The other sample comprised flakes removed from the anode interior upstream surface.

The final group of three samples in Table IV were standard samples of the composite metal alloys used in fabricating the discharge chamber components. Within the error in the analytical determinations, the results of these three analyses agreed with the composition specifications for the three types of steel.

The observation was made that all of the anode coating and coating flake samples spectrographically analyzed in this work, whatever their origin, were significantly magnetic.

Samples of the sputter-coated anode were prepared for analysis and inspection by cutting a second lengthwise strip from the anode, then sectioning this into five pieces. In preparing the samples, flakes of the sputtered material coating the strip spalled off near the edges. This tendency was particularly marked in the case of sample 1, cut from the downstream end of the anode, and left the coating edge appearing as shown in Figure 13(a), which was taken with the SEM at 100 times magnification. To obtain substantial areas of raised or spalled-off flakes on the remaining samples, so that the flake edges and the exposed substrate could be examined and analyzed, these samples were bent several times back and forth. The flakes thus removed were significantly smaller and much more tightly attached to the substrate in the case of samples 2 through 5 than for sample 1. Since partial flake layers may also have been detached during preparation of the samples, the possibility cannot be ruled out that the coating edges and flakes observed on the samples were of less than the original coating thickness and the observed coating surfaces were not the actual surfaces existing at the end of the tests.

A 3000 times magnified edge view of one of the sample 1 flakes shown in Figure 13(a) is seen in Figure 13(b) All the edge views were with the sample tilted 45° with respect to the scanning electron beam. A layered structure of the coating flake is clearly visible in Figure 13(b), with part of the upper layer missing at one point along the edge. Figure 13(b) demonstrates the great usefulness of SEM examination of sputtered coating flake edges and surfaces in determining flake thicknesses, the presence and thickness of individual layers in the flakes, and surface properties such as graininess, grain size, smoothness, and homogeneity. The examinations also permit the surface condition of the substrate beneath peeled coating flakes to be analyzed and characterized.

Figures 14(a) through (e) are edge views of coating flakes on anode samples 1 through 5 at 10,000 times magnification. The marked difference in surface smoothness and graininess between sample 1 and the others is evident. (However, the reduced edge thickness of the coating flakes on samples 2, 5, and possibly 4 suggests the possibility that the actual top layer and surface of each of these specimens may have delaminated prior to the SEM examination.)

The information obtained from SEM examination is summarized in Table V. The thicknesses and grain sizes were obtained by dimensional comparison with edge views of 3.8 μm thick platinum and 12.7 μm thick tantalum foils. The coating edge thicknesses determined ranged from 1.1 to 5.3 μm, the thickest being on the downstream end (sample 1) and the thinnest on the upstream end (sample 5); typical surface grain dimensions were in the range of 0.6 to 4.3 μm; and two layers, of inconsistent thicknesses, were generally visible in the edges of the coating flakes examined.

SEM X-ray analyses were run on the coating and substrate surfaces of all five anode samples, care being taken to insure that a homogeneous-appearing surface area not too close to a grossly different type of surface was viewed by the electron beam in each analysis. Usually the substrate analyses were performed on surface areas near, but not under, peeled or raised coating flakes.

Because of the general prevalence of stainless steel in the surfaces analyzed, a calibration analysis was performed on a sample of type 304 stainless cut from an unused thruster body. The spectrum obtained is shown in Figure 15(a) with counts per channel plotted against X-ray energy in keV. A typical coating analysis spectrum, that of anode sample 1 (from the downstream end of the anode), is shown in Figure 15(b) for comparison. The elements and X-rays detected in the various SEM analyses in this investigation are given in Table VI, with the strongest X-ray indicated for elements having more than one detectable X-ray.

The only spurious element detected in the analyses was aluminum. Its detection, by the single X-ray at 1.5 keV, was due to the aluminum sample blocks on which the specimens were mounted for examination. When a specimen showing such an aluminum peak in its analysis was mounted on a carbon sample block and reexamined, the aluminum X-ray disappeared.

In Table VII are compiled various X-ray peak height ratios found in the analyses of the five anode coating samples and their substrates. In all cases the strongest detected X-ray of each indicated element (see Table VI) is the one compared. All but two of the ratios involve iron as the standard element. Also included in Table VII are the values for the same ratios from the analysis of the standard stainless steel specimen.

Each ratio is not equal, but should be nearly directly proportional, to the concentration ratio of the two elements in the surface layer analyzed.

One deduction useful in interpreting the SEM X-ray ratios is that since stainless steel is the only source of chromium in the thruster, the amount that the chromium/iron (Cr/Fe) ratio is less than the standard stainless steel value of 0.44 measures the excess iron present over the stainless steel contribution. The source of this essentially pure iron must be the type 1010 mild steel parts in the discharge chamber. Similarly, the amount that the nickel/chromium (Ni/Cr) ratio is greater than the standard stainless steel value of 0.20 measures the excess nickel present over the stainless steel contribution. The only possible source of this is the nickel plating of the anode pole piece insert. It was consistently found in several comparisons (included in Table VII) that the coating X-ray analysis results did not depend on the size of the coating area analyzed, so long as the whole area was homogeneous in appearance. Sample areas differing by a factor of ten were examined in making such comparisons. This result tends to indicate that the coating surfaces comparatively analyzed, which were located away from flake edges, were the true surfaces existing at the end of the final test in the investigation and had not undergone significant delamination during preparation of the samples. A few SEM X-ray analyses were performed on well-separated areas on the same coating sample and did yield perhaps significantly different spectra. These results are included and are evident in Table VII.

Comparative Examinations of Endurance Test Anode Coating and Flakes

Several comparative analyses and SEM examinations were performed on anode flakes and the interior anode coating from the 9715-hr endurance test. The emission spectrographic analyses of one sample of flakes removed from the upstream interior anode surface and of two samples of flakes found resting on the discharge chamber side of the screen grid have already been presented. The results of these three analyses (see Table IV) are sufficiently in agreement to conclusively establish that the flakes found on the screen grid, which ultimately were responsible for the termination of the endurance test, had peeled from the upstream interior surface of the anode. Visual examination of these flakes and the anode also confirmed this conclusion, as there were many regions on this surface from which flakes had obviously peeled.

To obtain anode coating samples from the endurance test for SEM examination, two adjacent coating flakes of substantial size were removed from the upstream interior edge of the anode after being loosened by slight flexing of the edge. The coating adhesion to the substrate was clearly quite poor in this region, judging from the ease with which the coating flakes were loosened from it, and large flakes (>0.7 cm in one dimension) could easily be detached. It appeared that the flakes removed for examination comprised the entire surface coating at their locations. However, nearby areas were visible where the coating itself had evidently delaminated with the exterior surface peeling or flaking off and the interior layer(s) of the coating remaining attached to the substrate. One of the two flakes removed for examination was mounted so its under surface could be investigated. Even in visual appearance the top and bottom flake surfaces were different, the former being gray and the latter brown in color.

For a coating flake from the downstream end of the interior anode surface, it was found much more difficult to loosen or break off coating flakes from the substrate by flexing the edge of the anode. Flakes so obtained were much smaller (<~0.2 cm in longest dimension) than those obtained from the other end of the anode. In mounting the downstream flake for examination of its top surface, a small portion of it broke off and was mounted with its under side up immediately adjacent to the main fragment. Thus both the top and bottom surfaces of the downstream flake could be examined.

Besides the above coating samples two small pieces were cut from the endurance test anode, one from the upstream and one from the downstream edge, and were mounted for examination of their interior surfaces. Due to the mechanical stress in cutting these specimens from the anode, much spalling of coating flakes and layers from the samples occurred, particularly from the upstream edge piece. It thus appeared quite likely that typical coating flakes observed on these samples would not be representative of the undisturbed anode coating at the conclusion of the endurance test but rather would show the coating which existed at some earlier stage of the test.

The apparent strength of coating adhesion to the anode substrate, as a function of position along the anode interior surface, was clearly reversed between the ΔV_I tests and the endurance test. In the ΔV_I tests the sputter-deposited coating was least adherent to and most likely to flake off from the downstream end of the anode. In the endurance test the coating was least adherent to and did, in fact, flake off from the upstream end of the anode.

All the coating flakes which were removed or which spalled from the endurance test anode in preparing the specimens for SEM examination were found to be quite strongly magnetic, as were all the spectrographically analyzed coating flake samples obtained from this thruster.

Figure 16(a) shows an edge view and Figure 16(b) a surface view of the upstream anode flake from the endurance test, mounted top side up, both SEM pictures being taken at 1000 times magnification. From the edge view the flake thickness was measured to be 14 μm. The edge view also reveals at least eight layers in the flake, with thick layers being separated by thin layers. A particularly well-defined bottom layer is seen from the fact that a narrow width of it along the edge has delaminated from the adjacent coating with which the flake was contiguous before being broken off. Typical surface grain dimensions in Figure 16(a) are about 3 μm, in Figure 16(b) about 6 μm.

Figure 17(a) shows an edge view, at 3000 times magnification, and Figure 17(b) a surface view, at 1000 times magnification, of the upstream anode flake mounted under side up. The difference in surface appearance between the underside shown in these views and the top side of these flakes shown

in Figures 16(a) and (b) is striking, the under surface being undulating and almost devoid of μm-size or larger grains. The edge thickness measured from Figure 17(a) is 11 μm, and again the layers in the flake are evident, though less well defined than in Figure 16(a). On close examination the layers seen in Figure 17(a) match up well in order and thickness with those seen in Figure 16(a), starting with the bottom layer of the latter figure and working up, except that approximately the top three layers evident in Figure 16(a) are missing from the flake shown in Figure 17(a). This accounts for the observed difference in thickness between the two flakes. This layering comparison and agreement is shown in Table VIII, which lists all the information obtained from SEM examination of the endurance test anode flakes and specimens concerning flake thickness, layers and layer thickness in the flakes, and typical surface grain dimensions.

An edge view of the underside-up fragment of the downstream anode flake from the endurance test is shown in Figure 18(a) at 1000 times magnification. The bottom surface shows very much the same smooth, grain-free appearance as does the bottom surface of the upstream flake seen in Figures 17(a) and (b). The flake thickness is calculated to be 22 μm, and the flake edge reveals at least four layers, with the original bottom layer again partly delaminated from the rest of the flake near the right-hand edge. As may be seen from Table VIII, however, the layer order and thicknesses only partially match those found in the upstream flake.

The top surface of the downstream anode flake is shown in Figure 18(b) at 1000 times magnification. This view reveals a very granular surface, with typical grain size dimensions of ~5 μm. Moreover, the surface structure appears very different from that of the upstream flake top surface seen in Figures 16(a) and (b) at the same magnification, as the downstream flake shows an almost totally granular structure with many crevices while the upstream flake shows isolated grains on an otherwise quite smooth, grain- and crevice-free coating surface.

Figure 18(c) shows an edge view, at 1000 times magnification, of a raised coating flake on the downstream section cut from the endurance test anode. From the calculated flake thickness of 29 μm and the close similarity of the surface appearance to that shown in Figure 18(a), it is concluded that none of the flake is missing in this view. Again a well-defined bottom layer of the flake is visible by the projecting delaminated portion seen toward the left of the figure. No other layers besides this and the granular top surface layer are evident. A typical grain dimension of 6 μm in the top surface was measured from Figure 18(c), about the same as found in Figure 18(b).

It may be noted that in the endurance test coating samples and flakes examined, the bottom coating layer showed a tendency to delaminate from the rest of the coating in all four flake edge views in which it was observed.

A definite increase in coating and flake thickness is indicated between the upstream and downstream ends of the endurance test anode by the SEM measurements compiled in Table VIII. Flake thicknesses of 10, 11, and 14 μm were determined for the various upstream specimens, with the 11-μm measurement indicated to be low by about 3 μm due to missing top surface layers, while flake thicknesses of 22 and 29 μm were determined for the two downstream specimens.

The results obtained from SEM X-ray analyses of the various endurance test anode and anode coating flake specimens are compiled in Table IX, in the form of the same X-ray ratios tabulated in Table VII. Some of the more striking spectra observed are shown in Figures 19(a), (b), and (c), taken respectively of the top surface of the downstream coating flake, the (top) surface of the coating on the downstream anode section, and the under surface of the downstream coating flake. The top surface of the flake may be seen from Figure 19(a) to show essentially nothing but iron in its X-ray spectrum. The bottom surface of the flake shows an extremely strong molybdenum X-ray signal, with relatively weak iron and nickel, and even weaker chromium X-rays in its spectrum, Figure 19(c). The molybdenum/iron (Mo/Fe) ratio increases by a factor of over 200 between the top and bottom surfaces of the flake. The spectrum of the coating on the downstream anode section, Figure 19(b), displays an intermediate situation with nearly equally strong molybdenum and iron X-ray peaks. This is not too surprising in view of the extensive spalling of the top coating surface which was observed during preparation of the anode section for SEM examination. As seen in Table IX, a definite trend in the Ni/Fe X-ray peak ratios also exists among the three downstream specimens, with higher values of this ratio accompanying higher Mo/Fe ratios.

SEM X-ray analyses of the two flakes and one coated specimen from the upstream end of the anode revealed quite similar, but less pronounced trends in the X-ray ratios (Table IX). For these specimens the increase in the Mo/Fe ratio between the top and bottom flake surfaces is only about a factor of five, with the upstream anode coating sample again showing an intermediate value. With respect to the Ni/Fe, Cr/Fe, and Ta/Fe X-ray ratios found, however, it is the top flake surface of the three upstream coating specimens examined which occupies the intermediate position.

A significant conclusion may be drawn from the two substrate analyses included in Table IX. These were performed on exposed substrate regions of the upstream and downstream anode samples quite near the coating areas analyzed. If the X-ray ratios obtained in these analyses are compared with those from the analysis of the standard specimen of type 304 stainless steel (of which the anode was fabricated), it will be noted that the Ni/Fe ratios are 60-90 percent higher, the Ni/Cr ratios 65-110 percent higher, and the Cr/Fe ratios slightly lower in the substrate analyses. This indicates that the substrate surfaces from which the coating flakes peeled or spalled off were themselves coated with a significant amount of nickel and a smaller amount of iron.

The results of the SEM X-ray analyses performed on the endurance test anode coating specimens will be considered further in the Discussion section.

Beam Profile Measurements

As previously described, beam current density

profiles were taken of the thruster used in this investigation during the first test (with ΔV_I = 39.6 V), under the standard, nominal thruster operating conditions listed in Table I. The measurements were taken with the beam probe traversing the beam in a plane just over 12-cm downstream from the grid system. The current density profiles found in the horizontal and vertical midplanes containing the thruster (and beam) axis are shown in Figure 20. The data plotted were interpolated from the probe data obtained at 0.635-cm intervals in the beam probe position during several traverses of the beam. The beam profiles found and plotted in the figure closely approximate a normal error curve over the whole width of the beam, with the error curve characterized by a standard deviation of about 3.2 cm.

IV. Discussion

Erosion-Deposition Mass and Composition Balances

To obtain a complete quantitative description of the erosion which took place in the discharge chamber during these tests, it is necessary to estimate the mass erosion from the upstream surface of the screen grid. It could not be readily disassembled from the vector grid assembly and weighed independently. The weight losses determined for the vector grid assembly include erosion of the screen grid and the accelerator. The weight change of the downstream surface of the screen grid was taken to be zero, from visual inspection. From the data in Table I, the average neutral propellant flow rate in the beam, obtained by subtracting the beam current J_B from the total cathode flow rate $\dot{m}_C$, was 16.6, 11.1, and 10.0 mA for the three tests at ΔV_I = 36.6, 39.6, and 42.6 V, respectively. The ratio of these values, 1.66:1.11:1.00, may be compared with the ratio of the accelerator drain currents J_A listed in Table I. Since the charge exchange ion erosion of the accelerator grid system should be approximately proportional to the neutral propellant flow rate in the beam, the close agreement of the ratios indicates that nearly all of the accelerator grid system erosion was by charge exchange ions. This conclusion is consistent with the grid system erosion observed.

If the ratio of the material weight eroded from the upstream screen grid surface is in the same general range as the ratios given in Table III for the other discharge chamber components and if the ratio of the accelerator grid system weight eroded is the same as that of the accelerator drain currents, a self-consistent division of the total weight loss of the vector grid system into accelerator and screen grid contributions may be obtained. This breakdown is shown in Table X, together with the various ratios referred to.

If the screen grid mass erosion estimate given in Table X is added to the measured weight losses for the rest of the discharge chamber components, as given in Table II, it will be found that 79, 87, and 84 percent of the observed thruster body-anode weight gain may be accounted for in the tests at ΔV_I = 36.6, 39.6, and 42.6 V, respectively. For the three tests taken as a whole, 84 percent of the total thruster body-anode weight gain is thus accounted for.

The comparison of total mass erosion/weight gain of the thruster body-anode may be extended to a composition comparison as well. To do this it is first necessary to estimate the fraction of the total cathode pole piece erosion attributable to each construction material used in the pole piece assembly. From visual inspection, erosion of the tantalum screen was taken to be zero. The erosion of the stainless baffle screw and support wires was from observation confined to the exposed end of the screw, and the total mass eroded during the tests was estimated to be 13.4 mg from the measured dimension changes of the screw. (See Figures 6(a) and (b) and the screw tip diameter measurements in Table II.) Thus the remainder of the total measured weight loss of 44.15 mg from the cathode pole piece during the tests consisted of type 1010 mild steel from the pole piece proper.

With the above material breakdown of the cathode pole piece erosion and the previous estimates of the upstream screen grid surface erosion, the gross overall weight composition of all the material known and estimated to have been sputter eroded from the discharge chamber surfaces and components during the three ΔV_I tests can be calculated. This has been done for iron, molybdenum, nickel, chromium, tantalum, manganese, and copper, which are all of the elements contributing $\geq$0.1 percent of the total. In the calculations, the emission spectrographic analyses shown in Table IV were taken for the composition of the type 302 stainless and type 1010 mild steel present in the components. The detailed results of the calculations are included in Table XI. For the anode pole piece insert, the eroded material is pure nickel, since the nickel plating on this component was not penetrated by the erosion.

The calculated composition in Table XI may be compared with the actual emission spectrographic analyses shown in Table IV of the sputter-deposited coating samples. It will be seen that the calculated weight percent concentrations of iron, nickel, and molybdenum in the bulk composition, these being the three principal constituents, are in quite good agreement with weighted average or interpolated compositions from the anode coating analyses. The calculated copper concentration also agrees satisfactorily with the results of the emission spectrograph analyses. However, the calculated chromium and manganese concentrations are both higher than those actually found in the anode coating samples and the calculated tantalum concentration is several times as high as that actually found. Despite the partial disagreements, the above comparison demonstrates the basic consistency in composition between that found for the sputter-deposited anode coating and that calculated from the masses and compositions of the material sputter eroded from the discharge chamber components. This consistency in composition complements the general agreement previously found between the total component weight loss and the thruster body-anode weight gain in the tests.

The above composition comparison is subject to the complication that all of the anode coating flake samples collected and analyzed to give the results shown in Table IV included sputter deposited material accumulated during the ~600 hours operation of the thruster prior to the start of the present investigation. As previously indicated though, the thruster was operated during nearly all of this time at conditions closely approximating those of the first ΔV_I test (with ΔV_I = 39.6 V).

Thus from the erosion rate ratios given in Table III it may be estimated that about 30 percent of each anode coating flake sample consisted of material deposited during the period of prior operation. The above composition comparisons are therefore believed still to be valid, with the prior thruster operation viewed as affecting the analytical results in Table IV the same as an extension in the duration of the ΔV_I = 39.6 V test would have. This test was the most nearly average test in the investigation.

As seen above, a consistent deficit was observed between the total weight loss of the discharge chamber components and the thruster body-anode weight gain in each of the tests. Taken with the general agreement found between the calculated bulk sputtered material composition and the anode coating chemical analyses, this strongly implies that essentially all of the material sputter-eroded inside the discharge chamber remains there and eventually deposits on the thruster body-anode assembly.

It is of considerable interest to explore the possible origins of the ~20 mg of the total thruster body-anode weight gain, which is unaccounted for by the measured and estimated erosion of the discharge chamber components. One probable source of some of the extra ~20 mg lies in the four screws, made of type 302 stainless steel, which attach the cathode-isolator-vaporizer assembly to the thruster backplate. As mentioned, the ends of these screws extend significantly into the discharge chamber in a region observed on the backplate to be subject to heavy erosion (see Fig. 8). If all of the ~20 mg of thruster body-anode weight gain unaccounted for originated from these screws, however, the Table XI bulk chromium concentration calculated in the sputtered material would be raised from 42. to about 6.4 percent. This would make its discrepancy with the Table IV analyses of the anode coating flake samples even larger. On the other hand, the additional iron, nickel, and molybdenum from the screws would not alter the agreement or consistency between the calculated bulk concentrations and the analytical results for these elements.

Another possible source of part of the extra 20 mg unaccounted for is molybdenum eroded from the accelerator grid system. Molybdenum atoms sputtered from the sides of the accelerator grid members by direct ion impingement could enter the discharge chamber on direct trajectories through the screen grid holes. However, only up to a maximum of about 8 mg of additional molybdenum could be accommodated in the sputtered material available for deposition in the discharge chamber before the calculated bulk molybdenum concentration in Table XI would be raised so high as to be in definite disagreement with the Table IV analyses of the anode sputter coating samples. (This 8-mg limit also includes any additional molybdenum eroded from the upstream surface of the screen grid in excess of the estimates previously made.) From Table X the estimated total mass eroded from the accelerator grid system in the three tests is about 87 mg; by this reasoning less than 10 percent of this could have entered the discharge chamber.

Another observation supporting the minimal contribution of molybdenum eroded from the accelerator grid system to the inventory of sputtered material available for deposit in the discharge chamber is the observed absence throughout the tests of any sputtered material deposits on the downstream surface of the screen grid. This surface, like the screen grid holes, presents a substantial view factor for material sputtered from the sides of the accelerator grid members.

The absence of any observed sputter deposits on the downstream surface of the screen grid also argues strongly against back-sputtered stainless steel from the tank walls and beam target as a possible source of the unaccounted-for 20 mg of thruster body-anode weight pickup. In addition, this source would increase the calculated bulk chromium concentration in the sputtered material inventory to a value even more in excess of the actually detected concentrations in the anode coatings, just as in the previously considered case of the screws through the thruster backplate.

The only other possible sources of sputtered material which could significantly contribute to the unaccounted-for 20 mg of the thruster body-anode assembly weight gain are the tantalum keeper cap and the tungsten-2 percent thoria tip of the main cathode. Since the calculated bulk tantalum concentration in the sputtered material available for deposition, as given in Table XI, is already several times greater than the tantalum concentration deteremined in any of the anode coating analyses shown in Table IV, the keeper cap is ruled out as a source of additional sputtered material. Similarly, since no definite presence of either tungsten or thorium was established in any of the anode coating or thruster body deposit analyses, the cathode tip may be eliminated as a possible source of additional sputtered material in the discharge chamber.

The principal conclusions thus drawn from the erosion-deposition mass and composition balances discussed in this section are, first, that essentially all the material sputter-eroded from the components and surfaces inside the discharge chamber remains inside the discharge chamber, ultimately to deposit on the anode and the thruster body, and, second, that little sputter-eroded material from outside the discharge chamber, specifically from the accelerator grid system, enters the discharge chamber and contributes to the sputter deposits formed. In other words, this study indicates that under the range of conditions here investigated in a 5-cm thruster, there is essentially no transport of sputtered material from inside to outside the discharge chamber through the grids and only a relatively small amount of sputtered material (compared with that generated in the discharge chamber) transported from outside to inside the chamber.

Sputtering Species

Singly and doubly charged mercury ions (Hg^+ and Hg^{+2}) are the two possible ionic species available in the discharge chamber which could cause the observed sputter erosion of the discharge chamber components in this work. The mechanism of the sputter erosion clearly lies in the electrostatic acceleration of the responsible ionic species across the plasma boundary sheath separating the main discharge plasma from the component being eroded. The exact magnitude (or range in magnitude)

of the accelerating potential drop available in the boundary sheath is not known in the 5-cm thruster but by analogy with results found in larger thrusters,[7] the plasma potential or the plasma side of the sheath may be taken to be within a volt or two of the anode potential, so that with the sputtered surfaces being at the cathode potential the sheath potential drop should generally be within 1-2 V of ΔV_I. Hence the sputtering ions will have an energy in eV equal to ΔV_I if they are Hg^+ ions or twice this energy if they are Hg^{+2} ions.

In the absence of available information on the sputter yields of low energy Hg^{+2} ions, the approximation will be made that these sputter yields are the same as those of Hg^+ ions having the same energy. Then from the data given by Askerov and Sena[8] on the sputter yields obtained from low energy Hg^+ ion bombardment of iron, tantalum, and nickel, ratios of the sputter yields expected in the three tests at different ΔV_I values in the present work may be constructed, under the alternative assumptions of erosion either by Hg^+ or by Hg^{+2} ions. Such ratios are presented in Table XII for the three elements mentioned, with the sputter yields estimated for the ΔV_I = 36.6 V test taken as the bases for the comparisons.

Since the beam current and accelerating voltages were held constant throughout the ΔV_I tests (while the ΔV_I was varied), it may be assumed that the Hg^+ ion densities and distribution also were nearly constant. Under the assumption that Hg^+ ions are the sputtering species, the yield ratios presented in Table XII for Hg^+ ions should agree with the erosion rate ratios observed for the various discharge chamber components and presented in Table III. As is evident, the Table XII yield ratios for Hg^+ ions definitely do not agree with the observed erosion rate ratios in Table III, leading to the conclusion that Hg^+ ions were not the predominant sputtering species in the present investigation.

A further qualitative argument against Hg^+ ions as the principal sputtering species lies in the fact that the ΔV_I values employed in these tests were barely sufficient to provide the Hg^+ ions in the discharge chamber with enough energy to exceed the tantalum sputtering threshold of 35 eV found by Askerov and Sena.[8] In contrast, these ΔV_I values were sufficient to provide the Hg^+ ions with sputtering energies substantially greater than the 12- and 9-eV sputtering threshold energies reported by the same authors for iron and nickel, respectively. Yet all the thruster discharge chamber components (apart from the anomalous case of the mild steel backplate) showed roughly the same erosion rate ratios in Table III for the three ΔV_I tests, regardless of whether the sputtered material of construction was tantalum, iron (including stainless steel), or nickel. This similarity in erosion rate ratios is inconsistent with the conclusion that the eroding species has barely more than the minimum energy necessary for any sputtering at all of one of the materials.

As subsequently will be mentioned, the high tantalum contents found in the emission spectrographic analyses of anode coating flakes from the 9715-hr endurance test also argue strongly against Hg^+ ions as the predominant sputtering species. Kerslake[9] has presented yet another argument, based on ion heating considerations and the baffle erosion observed during the same endurance test, which further denies the hypothesis of Hg^+ ion erosion of the discharge chamber components and supports the alternative conclusion that Hg^{+2} ions are the eroding species.

If Hg^{+2} ions were the principal discharge chamber sputtering species in the ΔV_I tests of this investigation, the discharge chamber components would not be expected to show erosion rate ratios agreeing with the Hg^{+2} sputtering yield ratios shown in Table XII for iron, tantalum, and nickel. The production rate of Hg^{+2} ions in ion thrusters is known to vary sensitively with ΔV_I at discharge voltages in the range of 35 to 45 V. To test the consistency of the Hg^{+2} erosion theory with the erosion results obtained in the present tests, the erosion rate ratios given in Table III for each component have been divided by the corresponding Hg^{+2} sputter yield ratios in Table XII for the appropriate construction material (taking iron as the construction material of the stainless steel components). The ratios thus obtained, given in the lower part of Table XII, should agree with the ratios of the Hg^{+2} ion densities, hence production rates, in the three ΔV_I tests. The ratios included in Table XII are for the cathode pole piece, the baffle, the baffle holddown nut, and the anode pole piece insert. Calculated ratios for the other components have been omitted because of (1) the large relative errors in the small erosion weight losses found for the cathode assembly shield, (2) the apparently anomalous erosion rate ratios found for the thruster backplate in the tests, and (3) the inclusion of accelerator grid erosion in the measured vector grid assembly weight losses. The rough agreement of the Table XII Hg^{+2} ion production rate ratios calculated from the erosion of the four discharge chamber components may be noted.

From considerations and results given by Milder and Sovey[10] and by Masek,[11] it may be concluded that the only Hg^{+2} production reaction of importance under the thruster operating conditions obtained during the present experiments is the reaction Hg^+ (ground state) $\xrightarrow{e^-}$ Hg^{+2} (ground state), in which e^- refers to a primary electron causing the indicated ionization. The minimum electron energy required for this reaction is 18.75 eV[10]. (Significant Hg^{+2} production by the direct double ionization reaction

$$Hg^0 \text{ (ground state)} \xrightarrow{e^-} Hg^{+2} \text{ (ground state)}$$

in the present series of tests is precluded by the ΔV_I range investigated and the high primary electron threshold energy required by this reaction.)

It has also been found[10] that the primary electron energy E_p (expressed in volts) may be related to ΔV_I by the equation

$$E_p = \Delta V_I - V_p$$

in which V_p is the plasma potential (in V) in the cathode-baffle region. For the present series of ΔV_I tests it is reasonable to take V_p as constant through the three tests and hence to expect the primary electron energy to increase by increments of 3 V in the tests, corresponding to the like increments in ΔV_I.

farthest downstream, with this perturbation acting to protect the components farther upstream.

Another discharge chamber component displaying the presumed sharply peaked radial ion density distributions of the discharge chamber in its erosion pattern is the thruster backplate, seen in Figure 8 following the first test. Here the region of severe erosion abruptly terminates at a diameter of 3.76 cm, indicating substantial departure of the radial ion density distributions from a Gaussian shape in this maximum upstream location in the discharge chamber.

Also consistent with the highly peaked, radial ion density profiles presumed to exist through most of the discharge chamber is the observed lack of erosion of the interior thruster body surface, which forms the outermost boundary of the discharge chamber. The erosion rate was low enough at this surface, in fact, that the sputter deposition rate over most of the surface was greater than the erosion rate and a net deposition of sputtered material took place on these surface areas. (See Fig. 9(b).)

The one thruster component located near the outside diameter of the discharge chamber which showed significant erosion during the tests by its weight losses was the anode pole piece insert. This erosion is presumed to be associated with the strongly concentrated magnetic field flux passing through the insert and into the discharge chamber, and possibly also with the proximity of the insert to the screen grid.

Conclusions From Anode Coating Examinations and Analyses

The magnified SEM edge view shown in Figure 13(b) of the coating flake on the number 1 anode sample from this study clearly displays a layered structure in the anode coating. This layered structure must correspond with and reflect the different operating and sputtering conditions prevailing during the three tests in this investigation. Hence, the clearly visible top layer, comprising about half the flake thickness, is interpreted as having been deposited during the final test, with ΔV_I = 42.6 V. Though not clearly evident, a thin layer of sputtered material deposited during the second test (at ΔV_I = 36.6 V) must be present below this top layer. The remaining thickness of the flake then would consist of material deposited during the first test (at ΔV_I = 39.6 V) and during the ~600 hours of thruster operation prior to the first test.

The smooth, relatively grain-free coating surfaces displayed in Figures 14(c), (d), and (e) of anode samples 3, 4, and 5 can be interpreted as reflecting a uniform, slow-to-moderate sputter deposition rate of very fine particle size material on the upstream portion of the anode (from which these samples were cut). In contrast, the very grainy, inhomogeneous appearance of the coating on the downstream sample 1, seen in Figure 14(a), may reflect a much more nonuniform, generally more rapid deposition of sputtered material, which was also of larger particle size. The coating surface on the anode sample 2, seen in Figure 14(b), seems to represent an intermediate case. Though the demarcation is not very clearly evident, the grainy, inhomogeneous character of the sample 1 coating surface in Figure 14(a) appears to extend in depth only to about half the thickness of the flake and hence may characterize only the final test in the investigation (at ΔV_I = 42.6 V). The lower half of the coating appears from the edge to more closely resemble the smooth coatings seen in Figures 14(c), (d), and (d), and the bottom of the coating flake may be surmised to be smooth. The coating flake thicknesses determined from Figures 14(a) through (e) for the anode coating samples and compiled in Table V are, as previously stated, not necessarily representative of the true coating thickness along the length of the anode, but the values obtained do tend to indicate that the coating thickness increases as the downstream edge of the anode is approached.

Several conclusions may be drawn from the results, summarized in Table VII, of the SEM X-ray analyses of the five anode coating samples and from the emission spectrographic analyses given in Table IV, of the anode coating and thruster body samples. It may be seen from both types of analyses that the Cr/Fe and Ta/Fe ratios found in the anode coating samples (taking X-ray peak ratios in the case of the SEM analyses and weight percent ratios in the case of the emission spectrographic analyses) remain fairly constant regardless of the location of the sample along the anode. Furthermore, this relatively constant Cr/Fe ratio is far lower than the ratio for type 302 stainless steel, indicating the presence in all the samples of considerable iron from the mild steel parts at the upstream end of the discharge chamber.

The complete list of sources for iron consists of the thruster backplate, the cathode pole piece, the baffle screw, and the baffle holddown nut. For chromium the only sources are the baffle screw and holddown nut, and for tantalum the baffle and the cathode assembly shield are the only sources. All of the above sputter sources for iron, chromium, and tantalum are located at the upstream end of the discharge chamber. The constant values found for the Cr/Fe and Ta/Fe ratios in the coating samples, together with their magnitudes, point to the definite conclusion that all of the sputter sources for iron, chromium, and tantalum act as a single point source of sputtered material, thus explaining why hardly any variation in the deposited ratios of these elements is found anywhere on the anode.

The constant Cr/Fe and Ta/Fe ratios noted above are particularly surprising for the upstream anode samples and coatings analyzed since the upstream end of the anode is in close proximity to the thruster backplate and has a much more favorable view factor for the backplate and the cathode pole piece than does the downstream interior anode surface. Thus it was expected that the upstream anode surface would collect more iron, relative to the chromium and tantalum it collected, than would the anode surfaces farther downstream. The actual result again emphasizes the sharp peaking of the Hg^+ and Hg^{+2} ion densities at the thruster axis and the consequent heavy concentration of erosion near this axis.

Another observation evident from the SEM analysis results in Table VII and the emission spectrographic analyses in Table IV is that the Ni/Fe and Mo/Fe ratios in the anode coating decrease rapidly with distance away from the downstream anode edge.

The source of the nickel is the nickel plating on the anode pole piece insert and the source of the molybdenum is the upstream surface of the screen grid (perhaps augmented by some molybdenum sputtered from the accelerator grid elements). Thus, the conclusion may be drawn that there is a definite, effective resistance within the discharge chamber to the transport of sputtered material upstream from the region of the screen grid. Furthermore, since there is no reason to expect a sharp decrease in the sputter deposition rates for iron, chromium, and tantalum on approaching the downstream edge of the anode, the high Ni/Fe and Mo/Fe ratios found in the coating in this region imply increased total deposition rates with distance downstream along the anode, due to the rise in the nickel and molybdenum contributions in the material deposited. This conclusion is in agreement with the previously noted trend in the coating thicknesses determined from the SEM coating edge views.

Conclusions From Comparative Endurance Test Examinations

The layers observed in the anode coating flakes from the 9715-hr endurance test are presumed to correspond with specific changes in the prevailing sputtering conditions. These changes, in turn, must correlate with alterations in the thruster operating conditions. Of the eight or more anode coating layers visible in the endurance test flake edge view shown in Figure 16(a), the partly delaminated bottom layer is of particular interest. As previously noted, a similar, partly delaminated bottom layer ranging in estimated thickness from 1.0 to 2.0 μm is also visible in the three other edge views of endurance test anode flakes shown in Figures 17(a), 18(a), and 18(c). This bottom coating layer probably was deposited during the first 2037 hours of the endurance test, at which point the thruster was removed from the test facility, exposed to air, equipped with the electrostatic vector grid assembly (in place of the translating screen vector grid assembly tested up to this point), and reinstalled for continuation of the endurance test. Thus, not only were the operating and sputtering conditions inside the discharge chamber suddenly changed at this point in the test by the presence of the new grid system but the sputtered material coating deposited on the anode to this time was exposed to the atmosphere, certainly causing some amount of surface oxidation. Both of these factors are likely to have contributed to the prominent demarcation and partial delamination of the bottom layer observed in the SEM flake edge views.

As distinguished from the mostly isolated grains visible on the upstream anode coating surfaces in Figures 16(a) and (b), the grains seen in Figures 18(b) and (c) on the top surface of the downstream coating flake and the downstream anode section from the endurance test form an almost continuously granular surface with many crevices and a large typical grain dimension (~5 to 6 μm). This type of coating surface is very similar to that seen in Figure 14(a) on the equivalently located downstream anode coating sample from the ΔV_I tests (though Figure 14(a) was taken at 10,000 times magnification, while Figures 18(b) and (c) were both taken at 1000 times magnification). Such a surface appearance suggests that more rapid, less uniform deposition of sputtered material, perhaps of larger particle size, took place on these regions. This more rapid, more granular deposition is certainly associated with the gross differences found between the composition of the anode coating at the downstream end of the anode and the composition at the upstream end. The indicated more rapid deposition of sputtered material at the downstream end of the anodes in both the endurance and the ΔV_I tests agrees with the trends in anode coating thickness indicated by the data in Tables V and VIII.

From the SEM X-ray analyses of the endurance test anode coating samples, it is clear that the thruster discharge chamber went through periods of very intense single component sputtering. This is the only tenable explanation of the nearly single element spectra obtained in some of the analyses, such as shown in Figures 19(a) and (c), since it is inconceivable that the continuous, normal sputtering of the other discharge chamber components ceased or changed much during these periods of nearly single element deposition.

The periods of high single component sputtering which can be identified in the endurance test from the SEM analyses include one at the beginning of the test when nickel from the nickel-plated anode pole piece insert predominated (with a significant contribution of iron from the mild steel components at the rear of the discharge chamber), a subsequent period when molybdenum from the screen grid (perhaps also the accelerator grid system) overwhelmed all the other elements being sputtered, and a period near the end of the test when iron from the mild steel anode pole piece insert, denuded of its nickel plating by sputter erosion, formed almost the single constituent in the sputtered material deposited on the downstream end of the anode. These periods were identified, respectively, from the SEM analyses of the substrate surfaces, the undercoating flake surfaces, and the top flake surfaces of the several coating samples analyzed. The existence of other periods during which a single discharge chamber component may have undergone severe sputter erosion is certainly not precluded.

The high tantalum content found in the emission spectrographic analyses and in most of the SEM X-ray analyses of the anode coating samples and flakes from the endurance test reflects severe erosion of the tantalum baffle during the test. As previously hypothesized, most of this probably took place after the baffle screw and holddown nut had been eroded down to the point that they no longer provided effective protection of the baffle from the eroding Hg^{+2} ions. Since this point was not reached in the ΔV_I tests of the present investigation, the tantalum content found in both the emission spectrographic and the SEM X-ray analyses performed on the coating samples from these tests was much lower.

The significant differences between the endurance test and the ΔV_I tests should be noted. The thrusters, following the installation of the electrostatic vector grid assembly on the endurance test thruster after 2037 hours of the test, were essentially identical. However, the endurance test thruster was operated throughout the test with an ion beam potential of +1300 V, an accelerator potential of -900 V, a nominal discharge potential ΔV_I of 38 V, and a beam current of 25 mA. The com-

parable values of these operating parameters during the ΔV_I tests are shown in Table I. The total effect of these operating condition differences, as far as the sputter erosion and deposition in the discharge chamber is concerned, is believed to be minor, though slightly higher erosion rates can be inferred in the endurance test from the 7 percent higher beam current. Of course the different values of ΔV_I chosen for investigation in the ΔV_I tests created major differences in the sputtering and deposition rates between the two thrusters.

The anode coating thicknesses found from the ΔV_I tests are in the range of 1 to 5 μm, with the larger thicknesses at the downstream end of the anode (see Table V). The anode coating thicknesses found from the endurance test are in the range of 10 to 29 μm, also with the larger coating thicknesses at the downstream end of the anode (see Table VII). The coating from the ΔV_I tests built up during a total of 1248 hours of discharge operation in the tests plus ~600 hours of prior operation. Thus this coating represents the sputter deposition from ~1850 hours of thruster operation, with almost half of the coating thickness indicated as having been deposited during the final 416-hr test at ΔV_I = 42.6 V. The anode coating from the endurance test accumulated during 9715 hours of operation, nominally at ΔV_I = 38 V. Thus, the ratio of total operating hours (during which anode deposition took place) was about 5:1 for the two experiments, while the ratio of anode coating thicknesses accumulated during the respective experiments was about 6 to 8:1.

Considering the erosion rate dependence on ΔV_I shown in Table III and Figure 4, the average anode deposition rate during the endurance test clearly was considerably higher than the rate predicted by the results of the ΔV_I tests for the nominal endurance test ΔV_I of 38 V. In fact, the average deposition rate during the endurance test was not much less than that found at ΔV_I = 42.6 V in the ΔV_I tests.

A possible explanation of this discrepancy in the anode sputter deposition rate lies in inaccuracies in the ΔV_I calibration and measurement during the endurance test or in substantial operation during the test at higher than nominal ΔV_I values. However, an equally possible and plausible explanation lies in the periods of high single component erosion identified previously as having occurred during the endurance test. Particularly during the final period of the test, as reported by Nakanishi and Finke,[5] abnormal operation conditions were frequently observed or required, and this period has been identified above as one during which unusually heavy erosion of the anode pole piece insert clearly occurred. It is also the period toward the end of which large anode coating flakes are known to have been resting on the discharge chamber surface of the screen grid, partially covering some of the grid holes and deleteriously affecting the main discharge operating characteristics. It is therefore quite likely that the anode deposition rate during the final period of the endurance test was substantially higher than the average rate before this period and that this abnormally high deposition rate at least partly explains the high overall average deposition rate during the endurance test and the observed discrepancy of this average rate with predictions from the ΔV_I tests.

The results given in Table IX for the SEM X-ray analyses of the endurance test anode coating samples and flakes support a conclusion previously derived from the comparable results of the ΔV_I tests. Relatively little sputtered material from outside the discharge chamber, specifically from the accelerator grid, enters the discharge chamber through the screen grid holes and contributes to the sputter deposition on the anode. The X-ray spectrum obtained from the top surface of the downstream anode coating flake and shown in Figure 19(a), or the X-ray ratios given for this analysis in Table IX, show an almost complete lack of molybdenum in the analyzed surface, relative to the iron present. This lack of molybdenum was observed in spite of the fact that the analyzed surface consisted of sputtered material deposited at the end of the endurance test, when the direct ion impingement erosion of the accelerator grid members is known to have been severe enough to have eroded through several of the grid memebers. The almost complete absence of molybdenum in the sputtered material deposited on the downstream anode surface when so much molybdenum was being sputtered from the accelerator grid members confirms the above conclusion that only a minimal amount of the material sputtered from the accelerator grid system enters the discharge chamber.

The SEM X-ray ratios obtained from the endurance test anode flake analyses also support another conclusion from the ΔV_I test results. An effective resistance exists in the discharge chamber against the upstream transport of sputtered material generated in the region of the screen grid. Examination of the Mo/Fe ratios obtained on the top and under surfaces of the upstream and downstream coating flakes (see Table IX) shows a definite resistance to the upstream movement and deposition of the predominant species being deposited. Iron from the anode pole piece insert shows this behavior in the case of the top flake surfaces and the molybdenum from the upstream surface of the screen grid shows it in the case of the under surfaces.

The emission spectrographic analyses performed on the anode and screen grid flakes from the endurance test may be seen from Table IV to show a very high tantalum content considering the small amount of tantalum present in the discharge chamber. As previously indicated, this tantalum originated from intense sputtering of the downstream baffle surface. The Table IV results show that the endurance test, conducted at a nominal ΔV_I of 38 V, yielded a much higher concentration of tantalum in the anode coating than did the ΔV_I tests in the present investigation, the one contributing the most to the anode deposition was conducted at ΔV_I = 42.6 V. If the reported[8] threshold energy of 35 eV for Hg^+ sputtering of tantalum is approximately correct, it is clearly impossible to explain the heavy baffle erosion observed during the endurance test and the high tantalum contents found in the coating flake analyses from the test on the basis of Hg^+ ions as the principal sputtering species. The observations and analyses support the conclusion that Hg^{+2} ions are the predominant sputtering species.

Spalling Tendency and Magnetism of Anode Coatings

The observations made on the spalling tendencies of the anode coatings from the ΔV_I test and from the 9715-hr endurance test were somewhat

contradictory. Both anode coatings demonstrated a much greater ease of spalling bigger flakes at one end of the anode surface, but no simple correlation could be established between the coating section which spalled the most readily and such properties of the coating as its relative thickness, composition, surface characteristics (including granularity), or location on the anode.

From the experimental results and observations, plus related considerations, however, some positive conclusions may nevertheless be tentatively drawn. The most likely physical situation in which large coating flakes will separate from their substrate is characterized by high cohesion and brittleness of the coating, low adhesion of the coating to the substrate, and the presence of a force tending to separate the two.

The cohesion and brittleness of the anode coatings is believed favored in general by uniform, fine-grained deposition of the coating material, to substantial thicknesses, on a coating surface which remains nearly smooth and free of large grains. The adhesion of the coating to the substrate is reduced with smoother substrate surfaces, smoother and more grain-free undercoating surfaces, and more dissimilar coating compositions and substrate surfaces (suggesting the importance of oxide layers on the substrate, for example). The forces most generally available for causing a coating separation are those arising from temperature changes with the coating and substrate having markedly different coefficients of thermal expansion.

The correlations between anode flake spalling tendency and the coating and substrate properties fairly well fit the observations and determinations made on the anode coatings from the ΔV_I and endurance tests. For example, see the top and under side views in Figures 16(a), 16(b), 17(a), and 17(b) of the most readily spalled coating section observed, which has a smooth grain-free surface.

As previously noted, a high molybdenum content was found from the SEM X-ray analyses in the under surface of the upstream anode flake examined from the endurance test. This may be the critical ingredient which, in conjunction with the other factors mentioned, led to the ready, spontaneous spalling of large coating flakes from the upstream anode surface during the endurance test. Not only does the molybdenum constitute a dissimilar material unlikely to bond strongly with the (nickel- and iron-coated) stainless steel anode substrate. More importantly, it establishes a major mismatch in the thermal expansion coefficients between the coating and the substrate, permitting any temperature change or cycling to create a force tending to spall the coating off. The comparable linear coefficients of thermal expansion for molybdenum and stainless steel at 200° C (an approximate operating temperature for the anode) are about $5.3 \times 10^{-6}/^{\circ}C$ and $16.5 \times 10^{-6}/^{\circ}C$, respectively.[16] The many thruster shutdowns, startups, and abnormal operating conditions which occurred during the latter stages of the endurance test provided an ample number of opportunities in which the differential thermal expansion stresses could have spalled off anode coating flakes. Such spalling is most likely to have occurred during thruster cooldowns.

The nickel and iron shown by the SEM X-ray analyses to be present on the stainless steel substrate surfaces of the endurance test anode coating specimens clearly demonstrated strong adhesion to the stainless steel of the substrate and much weaker adhesion to the molybdenum-rich under surface of the anode coating. The favored adhesion of surfaces having like chemical composition and thermal expansion properties is again demonstrated, as is also the unfavored adhesion of surfaces dissimilar in chemical composition and thermal expansion properties.

The observed strongly magnetic character the anode coatings from both the ΔV_I tests and the endurance test may well be of significant importance when the anode coating layer builds up to thicknesses such as found from the endurance test. Such a magnetic field conductor on the anode surface then would be able to abstract enough magnetic field lines from the main discharge volume to significantly lower the field strength in this volume and substantially shorten many of the electron trajectories to the anode, thus decreasing the propellant ionization efficiency and probably lowering the observed ΔV_I. Some performance degradation was observed in the final stages of the 9715-hr endurance test;[5] specifically, a moderate decrease did occur in propellant utilization, accompanied by a drop of about 1 V in the ΔV_I characteristic curve versus cathode keeper current and by a drop of about 2 V in the ΔV_I characteristic curve versus discharge current. However, the suggested magnetic field distortion by the anode coating is only one possible explanation of the observed changes. The potential for deleterious effects due to the magnetic character of a sputter-deposited coating on the anode should not be overlooked though.

Remedies for the Anode Coating Flake Problem

From the 9715-hr endurance test no inherent lifetime limitations for the critical discharge chamber components in the standard Hughes 5-cm thruster were found, even though the baffle screw and holddown nut were severely eroded. The limiting condition on endurance operation was the buildup of the sputtered coating on the anode and its spalling as large flakes therefrom.

One approach toward overcoming the anode coating problem is to substantially lower the sputtering rates of the critical discharge chamber components. This may be done in several ways. One, as proven by the results of the tests in this investigation, is to lower the standard operating ΔV_I from values near 40 V to values nearer to 35 V and keep the ΔV_I well controlled during thruster operation. Another possible way is to bias all or certain of the critical discharge chamber components, apart from the anode, to a potential somewhat higher than the cathode common potential, perhaps to the cathode keeper potential. This would correspondingly reduce the plasma sheath potential drop and hence, because of the reduced sputter yields, would substantially lower the Hg^{+2}-caused sputter erosion of these parts.

Another way to reduce the sputter erosion rates of the critical discharge chamber components is to make them of a more sputter-resistant material or to coat them with such a material. Carbon (graphite), tantalum, tungsten, molybdenum, various

oxide coatings, and even plastics are possible highly sputter-resistant materials which might be employed. Baffle assemblies and thruster backplates made of graphite are currently being tested to evaluate this method of reducing the component sputter erosion rates.

The exposed portion of the baffle screw and the baffle nut were found in the ΔV_I tests of this study and in the endurance test to apparently protect the baffle from substantial sputter erosion until the screw and the nut themselves were eroded away. Utilizing the same principal, sacrificial protective structures made of highly sputter-resistant materials, such as carbon, might be purposely designed and installed to protect otherwise heavily eroded components, including the baffle, the cathode pole piece, and the thruster backplate, from severe sputtering damage. Such protective structures might only need be of small size if optimally designed and optimally located in the discharge chamber.

Specific changes in the screen grid design or in the thruster beam optics, including as possibilities the use of a dished screen grid or different hole sizes or arrays, might substantially reduce the total erosion rate of the upstream screen grid surface by eliminating localized erosion of it. Such localized sputter erosion was clearly seen in the ΔV_I tests of this work. Localized screen grid erosion on the upstream side might also be eliminated or reduced by changing the thruster discharge characteristics, magnetic field, or radial ion distributions (in the discharge chamber).

Sputter erosion of the anode pole piece insert very likely could be reduced significantly by the use of an insert with a shorter conical section, which would thus extend a shorter distance into the main volume of the discharge chamber (see Fig. 1).

In all of the above proposals the aim is to substantially lower the sputter erosion rate of one or more critical discharge chamber component. Another obvious approach to solving the problem of sputter coating flakes spalling from the anode is to improve the adhesion of the anode coating so spalling does not occur. The specific reducation in the rate of molybdenum sputtering from the screen grid suggested above incorporates this approach. A similar method of achieving improved anode coating adhesion would be to make the screen grid of stainless steel or a nickel alloy or to plate the upstream surface of the screen grid with a similar material to a depth sufficiently thick that it would not be eroded through during the required duration of thruster operation. The material sputtered from the discharge chamber side of the screen grid would in either case be compatible with, highly adherent to, and well-matched in thermal expansion properties with the stainless steel anode substrate; hence the anode coating developed should likewise share these properties. However, the increased sputtering rate of the screen grid (surface) material, as compared with that of the molybdenum normally used, might result in such an increased rate of anode coating thickness build-up as to offset the advantage of the much improved coating adhesion to the anode.

A simple way of improving the adhesion of the anode coating would be to provide a rough substrate surface on the anode for it to adhere to. Carrying this idea one step further, Banks has proposed the fabrication of the anode from fine mesh screen material. Such an anode would be expected to develop a coating varying substantially in thickness over each mesh unit and correspondingly varying in adhesion to the substrate, with the thinner portions of the coating adhering well and the thicker portions adhering more poorly. With such a variation in coating adhesion over each mesh unit, no coating flakes larger than the mesh dimension or a few times it would be expected to spall off. If the mesh dimension were made sufficiently small, therefore, the spalled coating flakes would create none of severe problems caused by the centimeter-size flakes which spalled from the anode near the end of the 9715-hr endurance test and which led to the termination of that test. The screen anode concept is presently being evaluated.

V. Concluding Remarks

A 5-cm mercury ion thruster of the Hughes Research Laboratories design, equipped with an electrostatic vector grid system, has been operated for 416 hours each at constant discharge voltages ΔV_I of 36.6, 39.6, and 42.6 V. The purposes of the tests were to measure the sputter erosion and deposition rates of the discharge chamber components as a function of ΔV_I, elucidate the sputtering species, and determine the origin of the sputtered anode coating material which flaked off the anode in a 9715-hr endurance test of a very similar 5-cm thruster, subsequently causing termination of the endurance test.

A beam current of 23.4 mA was maintained throughout the ΔV_I tests, which were conducted as nearly as possible at constant, standard operating conditions previously optimized for the thruster. The discharge propellant utilizations were 58, 68, and 70 percent during the tests at ΔV_I = 36.6, 39.6, and 42.6 V, respectively.

Similar sputter erosion characteristics were found after all the tests. The discharge chamber components most heavily sputtered, in decreasing order of weight loss, were found to be the cathode pole piece assembly, the thruster backplate, the anode pole piece insert, and the baffle holddown nut. The erosion rates of all the sputtered discharge chamber components, except the thruster backplate, were found to be roughly in the ratio of 1:3:5 for the tests ordered as to increasing ΔV_I. The weight gains of the thruster body-anode assembly, the only component to gain weight during the tests, were also in the same ratio for the three tests.

It was found that the measured weight losses of the eroded discharge chamber parts, plus reasonable estimates for the screen grid weight losses, accounted for 79 to 87 percent of the anode assembly weight gain during each of the tests. The bulk elemental composition of the sputtered discharge chamber material from the three tests, calculated from the weight losses and compositions of the eroded components, was found to be quite consistent with the results of emission spectrographic analyses performed on samples of the deposited anode coating.

It was concluded that essentially all the material sputtered from the discharge chamber components deposited on the anode and that very little

sputtered material from the accelerator grid system entered the discharge chamber through the screen grid. It was further concluded from scanning electron microscope (SEM) X-ray analyses that a substantial resistance to upstream flow of sputtered material from the screen grid region exists in the discharge chamber.

The discharge chamber components showed a consistent pattern of heavy sputter erosion concentrated near the thruster axis. This erosion pattern was found to agree with radial ion density distributions which could be extrapolated from beam current density profiles measured about 12 cm downstream from the thruster grids during the first ΔV_I test. The beam current density profiles were Gaussian-shaped and described by a standard deviation of about 3.2 cm.

From various considerations, including the reasonable agreement of Hg^{+2} production rate ratios calculated from the erosion results with a semi-theoretical prediction of the production rate as a function of the primary electron energy, it was concluded that the predominant sputtering species in the discharge chamber was Hg^{+2} ions.

Emission spectrographic analyses and SEM examinations of anode coating samples from the 9715-hr endurance test generally confirmed the conclusions from the ΔV_I tests. They also indicated periods of very high single component sputter erosion in the discharge chamber during the endurance test. The average anode deposition rate for the test was found to be considerably higher than that predicted from the ΔV_I tests on the basis of the nominal ΔV_I of 38 V during the endurance test. The strongly magnetic character of the anode coating from the endurance test was suggested as a possible explanation of the performance degradation observed during the latter stages of the test.

Tentative conclusions were reached concerning factors tending to cause spalling of coating flakes from the stainless steel anode; these include high molybdenum content, a smooth grain-free undercoating surface, and uniform, not-too-rapid deposition of a nongranular coating.

The scanning electron microscope was found to be a powerful tool for examining and analyzing sputtered coating samples and substrates, yielding highly useful information on grain sizes, coating and coating layer thicknesses, coating granularity, and elemental X-ray peak and composition ratios in the coatings and substrates.

VI. References

1. Hyman, J., Jr., "Design and Development of a Small Structurally Integrated Ion Thruster System," Oct. 1971, Hughes Research Labs., Malibu, Calif; also CR-120821, Oct. 1971, NASA.

2. Hyman, J., Jr., "Performance Optimized, Small Structurally Integrated Ion Thruster System," May 1973, Hughes Research Labs., Malibu, Calif., also CR-121183, May 1973, NASA.

3. Hudson, W. R., and Banks, B. A., "An 8 Cm. Electron Bombardment Thruster for Auxiliary Propulsion." Paper proposed for AIAA 10th Electric Propulsion Conference, Lake Tahoe, Nev., Oct.-Nov. 1973.

4. King, H. J., Collett, C. R. and Schnelker, D.E., "Thrust Vectoring Systems, Part I: 5 cm Systems," Final Report, 1970, Hughes Research Labs., Malibu, Calif.; also CR-72877, 1970, NASA.

5. Nakanishi, S., and Finke, R. C., "A 9700-Hour Durability Test of a Five Centimeter Diameter Ion Thruster." Paper proposed for AIAA 10th Electric Propulsion Conference, Lake Tahoe, Nev., Oct.-Nov. 1973.

6. Hyman, J., Jr., "SIT-5 System Development," AIAA Paper 72-492, Bethesda, Maryland, 1972.

7. Wells, A. A., "Current Flow Across a Plasma 'Double Layer' in a Hollow Cathode Ion Thrustor," AIAA Paper 72-418, Bethesda, Md.. 1972.

8. Askerov, Sh. G. and Sena, L. A., "Cathode Sputtering of Metals by Slow Mercury Ions," Fizika Tverdogo Tela, Vol. 11, no. 6, June 1969, pp. 1591-1597.

9. Kerslake, W. R., "Review of Kaufman Thruster Development at the Lewis Research Center - 1973," TM X-68202, 1973, NASA.

10. Milder, N. L. and Sovey, J. S., "Characteristics of the Optical Radiation from Kaufman Thrusters," TN D-6565, Nov. 1971, NASA.

11. Masek, T. D., "Plasma Properties and Performance of Mercury Ion Thrusters," JPL-TR-32-1483, June 1970, Jet Propulsion Lab., Pasadena, Calif.; also CR-110731, June 1970, NASA.

12. Gryzinski, M., "Classical Theory of Atomic Collisions. I. Theory of Inelastic Collisions," Physical Review, Vol. 138, No. 2A, Apr. 1965, pp. 336-358.

13. Dugan, J. V., Jr. and Sovie, R. J., "Volume Ion Production Costs in Tenuous Plasmas: A General Atom Theory and Detailed Results for Helium, Argon, and Cesium," TN D-4150, Sept. 1967, NASA.

14. Bechtel, R. T., "Component Testing of a 39-Centimeter Diameter Electron Bombardment Thruster," AIAA Paper 70-1100, Stanford, Calif, 1970.

15. Knauer, W., Poeschel, R. L., King, H. J. and Ward, J. W., "Discharge Chamber Studies for Mercury Bombardment Ion Thrusters," Sept. 1968, Hughes Research Labs., Malibu, Calif.; also CR-72440, Sept. 1968, NASA.

16. Smithells, C. J., Metals Reference Book, 4th Ed., Vol. 3, Plenum Press, New York, pp. 687, 700.

TABLE I. - CHARACTERISTIC OPERATING

CONDITIONS DURING TESTS

Discharge potential (ΔV_I), V	36.6	39.6	42.6
Ion beam potential[a] ($V_I + V_G$), V	1400	1400	1398
Accelerator potential (V_A), V	-700	-700	-700
Neutralizer coupling potential (V_G), V	-7	-7	-9
Beam current (J_B), mA	23.4	23.4	23.4
Accelerator drain current (J_A), mA	0.127	0.090	0.079
Emission current (J_E), mA	268	311	332
Hg cathode flow rate ($\dot{m}_C$), equiv. mA	40.0	34.5	33.4
Hg neutralizer flow rate ($\dot{m}_N$), equiv. mA	1.7	2.2	2.4
Cathode keeper potential (V_{CK}), V	14	14	14
Cathode keeper current (J_{CK}), mA	400	400	400
Cathode heater power, W	0	0	0
Discharge utilization, %	58.5	67.8	70.0
Discharge losses,[b] eV/ion	419	526	604
Discharge on time, hrs	416	416	416
High voltage on time, hrs	409	400	407

[a]Equals net accelerating potential V_I plus neutralizer coupling potential V_G (<0).
[b]Excluding cathode keeper losses and neglecting double ionization.

TABLE II. - 5-CM THRUSTER COMPONENT EROSION RATES

Component	Initial weight, g	ΔV_I = 36.6 V		ΔV_I = 39.6 V		ΔV_I = 42.6 V	
		Weight change, mg	Weight change rate,[a] μg/hr	Weight change, mg	Weight change rate,[a] μg/hr	Weight change,	Weight change rate,[a] μg/hr
Cathode assembly shield	5.35	-0.08	-0.2	-0.21	-0.5	-0.34	-0.8
Cathode pole piece assembly[b]	12.13	-4.40	-10.6	-13.78	-33.1	-25.97	-62.4
Baffle	0.27	-0.19	-0.5	-0.72	-1.7	-1.30	-3.1
Baffle holddown nut	0.09	-1.46	-3.5	-3.90	-9.4	-6.96	-16.7
Thruster back plate	41.66	-3.37	-8.1	-7.39	-17.8	-9.23	-22.2
Thruster body - anode	27.11	+15.31	+36.8	+39.48	+94.9	+71.15	+171.0
Anode pole piece insert	5.74	-1.85	-4.4	-5.75	-13.8	-7.96	-19.1
Vector grid assembly[c]	154.81	-39.	-94.	-28.	-67.	-31.	-75.
Measurement	**Initial value, mm**	**Change, μm**	**Change rate,[a] μm/hr**	**Change, μm**	**Change rate,[a] μm/hr**	**Change, μm**	**Change rate,[a] μm/hr**
Baffle screw tip diameter	0.88	-53.	-0.13	-110.	-0.26	-190.	-0.46

[a]Based on discharge operation time of 416 hrs/test.
[b]Includes baffle screw but not baffle or baffle holddown nut.
[c]Includes dual axis electrostatic vector accelerator grid, screen grid, and anode pole piece but not anode pole piece insert.

TABLE III. - RATIOS OF COMPONENT EROSION RATES

Component	Material of construction	Erosion rate ratios		
		$\frac{\Delta V_I = 39.6\ V}{\Delta V_I = 36.6\ V}$	$\frac{\Delta V_I = 42.6\ V}{\Delta V_I = 39.6\ V}$	$\frac{\Delta V_I = 42.6\ V}{\Delta V_I = 36.6\ V}$
Cathode assembly shield	Tantalum	2.6	1.6	4.3
Cathode pole piece assembly[a]	1010 Mild steel,[b] 302 stainless,[b] and tantalum[b]	3.1	1.9	5.9
Baffle	Tantalum	3.8	1.8	6.8
Baffle holddown nut	302 Stainless	2.7	1.8	4.8
Thruster backplate	1010 Mild steel	2.2	1.2	2.7
Thruster body - anode	304 Stainless	[f]2.6	[f]1.8	[f]4.6
Anode pole piece insert	Nickel[c] and 1010 mild steel[c]	3.1	1.4	4.3
Vector grid assembly[d]	Molybdenum[e]	0.7	1.1	0.8

[a]Includes baffle screw but not baffle or baffle holddown nut.
[b]Bulk of pole piece is 1010 mild steel; baffle screw is 302 stainless; pole piece screen is tantalum.
[c]Exterior plating is nickel; bulk of pole piece insert is 1010 mild steel.
[d]Includes accelerator grid, screen grid, and anode pole piece.
[e]Material of both grids; anode pole piece not significantly exposed to discharge.
[f]Ratio of weight gains.

TABLE IV. - EMISSION SPECTROGRAPHIC ANALYSES

Number	Sample	Weight percent of total metal content							
		Fe	Mo	Ni	Ta	Cr	Mn	Cu	Other ≥ 0.10
1	Anode coating, downstream	46	22	32	0.8	1.2	0.10	0.31	Co 0.28, Sn 0.14
2	Anode coating, middle	87	3.3	5.3	0.5	3.3	0.21	0.12	Sn 0.17
3	Anode coating, upstream	93	1.2	2.7	0.5	2.3	0.12	0.10	
4	Body deposit, downstream	50	5.4	41	2.6	0.86	0.07	0.10	Co 0.22
5	Body chips	88	5.2	2.3	2.2	0.97	0.11	0.25	Al 0.56
6	Body deposit, upstream	95	1.8	1.1	1.8	1.0	0.03	0.01	
7	Endurance test, screen grid flakes	44	21	16	14	4.4	0.04	0.15	
8	Endurance test, screen grid flakes	40	19	12	22	5.5	0.52	0.26	Co 0.13
9	Endurance test, anode flakes	41	28	10	15	5.1	0.08	0.13	
10	302 Stainless standard	72	0.4	8.4	[a]----	17.5	1.5	0.3	Co 0.1, V 0.1
11	304 Stainless standard	71	0.3	9.1	[a]----	17.6	1.8	0.1	V 0.1
12	1010 Mild steel standard	99	0.03	0.06	[a]----	0.01	0.13	0.03	

[a]Not detected.

TABLE V. - SCANNING ELECTRON MICROSCOPE EXAMINATIONS

OF ANODE COATING SAMPLES FROM ΔV_I TESTS

Number	Sample	Nominal magnification, times	Coating thickness, μm	Layer thicknesses,[a] μm			Typical grain dimension, μm
1[c]	Anode coating sample	10,000	3.4	1.4	0.8	---	1.1
		10,000	---	---	---	---	0.6
		3,000	5.3	2.6	1.8	0.9	---
			5.3	2.1	2.1	1.1	---
			---	---	---	---	1.3
			---	---	---	---	1.3
		1,000	3.8	1.6	2.2	---	0.6
		1,000	4.1	1.9	2.2	---	---
2		10,000	1.7	0.6	1.1	---	0.8
3		10,000	3.3	1.2	2.1	---	---
3		3,000	---	---	---	---	4.3
4		10,000	2.2	[b]1.4	[b]0.8	---	---
5[d]		10,000	1.1	---	---	---	[b]0.6
5		3,000	---	---	---	---	2.1

[a]Layers listed from bottom up.
[b]Poorly defined or questionable.
[c]Downstream end of anode.
[d]Upstream end of anode.

TABLE VI. - SCANNING ELECTRON MICROSCOPE X-RAY ANALYSIS PEAKS

X-ray energy, keV	Element	X-ray identification	X-ray energy, keV	Element	X-ray identification	X-ray energy, keV	Element	X-ray identification
0.8	Fe+Ni	L_α	[b]5.4	Cr	K_α	[a]8.2	Ta	L_α
1.5	Al	$K_\alpha+K_\beta$	6.0	Cr	K_β	[a]8.3	Ni	K_β
[b]1.7	Ta	M_α	[b]6.4	Fe	K_α	10.0	Hg	L_α
[a]2.3	Mo	L_α	7.1	Fe	K_β	[a]11.8	Hg	L_{β_1}
[a]2.4	Mo	L_{β_1}	[b]7.5	Ni	K_α	[a]11.9	Hg	L_{β_2}
						17.5	Mo	K_α

[a]Unresolved.
[b]Strongest X-ray detected from given element; used for intensity ratios.

TABLE VII. - SCANNING ELECTRON MICROSCOPE X-RAY ANALYSES

OF ANODE COATING SAMPLES FROM ΔV_I TESTS

Number	Sample	Magnification, times	X-ray peak height ratios					
			Mo/Fe	Ni/Fe	Cr/Fe	Ta/Fe	Ni/Cr	Mo/Ni
1[b]	Anode coating sample	30,000	0.84	1.8	0.18	0.06	9.9	0.47
		3,000	0.85	2.2	0.15	0.05	15	0.39
		3,000	1.21	1.7	0.14	0.10	13	0.70
		?	0.9	2.4	[a]0.14	0.07	[a]17	0.36
2		10,000	0.39	0.12	0.20	0.05	0.6	3.4
3		10,000	0.24	0.15	0.15	0.05	1.0	1.6
3		1,000	0.24	0.15	0.14	0.06	1.1	1.6
4		10,000	0.20	0.11	0.17	0.06	0.6	1.9
5[c]		3,000	0.08	0.07	0.15	0.07	0.5	1.2
5		300	0.10	0.06	0.14	0.07	0.4	1.8
1[b]	Anode sample substrate	10,000	[a]0.03	0.085	0.42	[a]0.02	0.20	[a]0.4
		3,000	[a]0.03	0.085	0.39	[a]0.03	0.22	[a]0.4
		3,000	[a]0.04	0.089	0.42	[a]0.02	0.21	[a]0.5
		?	[a]0.02	0.086	0.41	[a]0.02	0.21	[a]0.2
2		30,000	[a]0.02	0.085	0.43	[a]0.01	0.20	[a]0.3
3		30,000	0.16	0.095	0.21	[a]0.04	0.45	1.7
4		30,000	0	0.074	0.39	[a]0.01	0.19	0
5[c]		30,000	0.05	0.084	0.18	[a]0.02	0.47	0.6
	304 Stainless standard	3,000	0	0.085	0.44	0	0.20	0

[a]Large error in value.
[b]Downstream end of anode.
[c]Upstream end of anode.

TABLE VIII. - SCANNING ELECTRON MICROSCOPE EXAMINATIONS OF ENDURANCE TEST

ANODE COATING FLAKES AND SAMPLES

Sample	Nominal magnification, times	Coating thickness, μm	Layer thicknesses,[a] μm				Typical grain dimension, μm
Downstream anode coating flake, top side up	1000	----	---	----	---	---	5
Downstream anode coating sample		28.6	1.0	27.6	---	---	6
Downstream anode coating flake, under side up		22.2	2.9	3.5	9.4	6.4	---
Upstream anode coating flake, top side up		14.0	1.6 0.6	3.5 1.3	1.0 0.6	3.2 2.2	3
Upstream anode coating flake, top side up		----	---	----	---	---	6
Upstream anode coating sample		9.5	---	----	---	---	---
Upstream anode coating flake, under side up	3000	10.7	1.9	3.6	0.9	4.3	---

[a]Layers listed from actual bottom coating surface up, reading from left to right.

TABLE IX. - SCANNING ELECTRON MICROSCOPE X-RAY ANALYSES OF ENDURANCE TEST ANODE COATING FLAKES AND SAMPLES

Sample	Magnification, times	X-ray peak height ratios					
		Mo/Fe	Ni/Fe	Cr/Fe	Ta/Fe	Ni/Cr	Mo/Ni
Downstream anode coating flake, top side up	1,000	[a]0.03	[a]0.01	[a]0.01	[a]0.01	[b]----	[b]----
Downstream anode coating sample	3,000	0.77	0.08	0.08	[a]0.04	1.0	10
Downstream anode coating flake, under side up	10,000	6.6	0.86	[a]0.2	[a]0.2	[a]4	7.7
Upstream anode coating flake, top side up	30,000	0.42	0.29	0.10	0.14	3.0	1.4
	3,000	0.44	0.39	0.09	0.20	4.6	1.1
	1,000	0.42	0.39	0.09	0.18	4.5	1.1
Upstream anode coating sample	10,000	1.24	0.20	0.08	0.07	2.5	6.1
Upstream anode coating flake, under side up	1,000	2.17	1.00	0.21	0.31	4.7	2.2
Downstream anode sample substrate	10,000	[a]0.01	0.16	0.38	[a]0.01	0.42	[a]0.07
Upstream anode sample substrate	30,000	[a]0.03	0.14	0.41	[a]0.02	0.33	[a]0.23
304 Stainless standard	3,000	0	0.085	0.44	0	0.20	0

[a]Large error in value.
[b]Value meaningless.

TABLE X. - FITTED ACCELERATOR AND SCREEN GRID WEIGHT LOSSES IN ΔV_I TESTS

ΔV_I of test, V	36.6		39.6		42.6
Neutral flow in beam, $\dot{m}_c - J_B$, equiv mA	16.6		11.1		10.0
Ratio of neutral flows	1.66	:	1.11	:	1.00
J_A of test, mA	0.127		0.090		0.079
Ratio of J_A values	1.61	:	1.14	:	1.00
Total grid assembly weight loss in test, mg	39.		28.		31.
Fitted accelerator grid system weight loss in test, mg	38.2		25.5		23.
Ratio of accelerator grid system weight losses	1.66	:	1.11	:	1.00
Fitted screen grid weight loss in test, mg	0.8		2.5		8.
Ratio of screen grid weight losses	1.0	:	3.1	:	10.0

TABLE XI. - CALCULATED GROSS SPUTTERED MATERIAL COMPOSITION FOR COMBINED ΔV_I TESTS

Component	Construction material	Total component weight loss,[a] mg	Proportion of overall weight loss, percent	Amounts of elements eroded, mg						
				Fe	Mo	Ni	Ta	Cr	Mn	Cu
Cathode pole piece assembly	1010 Steel[b]	30.76	29.0	30.7	0.0	0.0	---	0.0	0.0	0.0
	302 Stainless[c]	13.39	12.6	9.6	0.1	1.1	---	2.3	0.2	0.1
Thruster back plate	1010 Steel	19.99	18.8	19.9	0.0	0.0	---	0.0	0.0	0.0
Anode pole piece insert	Ni[d]	15.56	14.7	----	---	15.6	---	---	---	---
Baffle holddown nut	302 Stainless	12.32	11.6	8.8	0.0	1.0	---	2.2	0.2	0.0
Screen grid	Mo	[e]11.3	10.6	----	11.3	----	---	---	---	---
Baffle	Ta	2.21	2.1	----	----	----	2.2	---	---	---
Cathode assembly shield	Ta	0.63	0.6	----	----	----	0.6	---	---	---
Totals		106.16	100.0	69.0	11.4	17.7	2.8	4.5	0.4	0.1
Weight percent composition				65.0	10.8	16.7	2.7	4.2	0.4	0.1

[a]For tests at all three ΔV_I values.
[b]Pole piece proper.
[c]Baffle screw and support wires.
[d]Plating material; substrate 1010 mild steel not eroded.
[e]Sum of estimated values from Table X.

TABLE XII. - MERCURY SPUTTER YIELD RATIOS AND CALCULATED PRODUCTION RATE RATIOS

Sputtered element	Sputter yield ratios for Hg^+ ions of indicated energies[a]		Component	Construction material	Calculated Hg^{+2} production rate ratios (for ΔV_I = 36.6: 39.6:42.6 V tests)
	Electron volt ratio	Electron volt ratio			
	36.6 : 39.6 : 42.6	73.2 : 79.2 : 85.2			
Fe	1.00 : 1.21 : 1.69	1.00 : 1:39 : 1.94	Cathode pole piece	Fe[b]	1.0 : 2.3 : 3.0
Ta	1.00 : 1.38 : 2.13	1.00 : 1.36 : 1.82	Baffle	Ta	1.0 : 2.8 : 3.8
Ni	1.00 : 1.28 : 1.62	1.00 : 1.18 : 1.41	Baffle hold-down nut	Fe[c]	1.0 : 1.9 : 2.5
Sputtering species	Hg^+	Hg^{+2}	Anode pole piece insert	Ni[d]	1.0 : 2.6 : 3.0

[a]Values read from curves of Reference 8 with slight extrapolation to obtain values for Fe at 36.6 and 39.6 eV and for Ta at 36.6 eV.
[b]Eroded material both type 1010 mild steel and type 302 stainless; all considered as Fe.
[c]Construction material type 302 stainless; considered as Fe.
[d]Eroded material all from Ni plating; substrate is type 1010 mild steel.

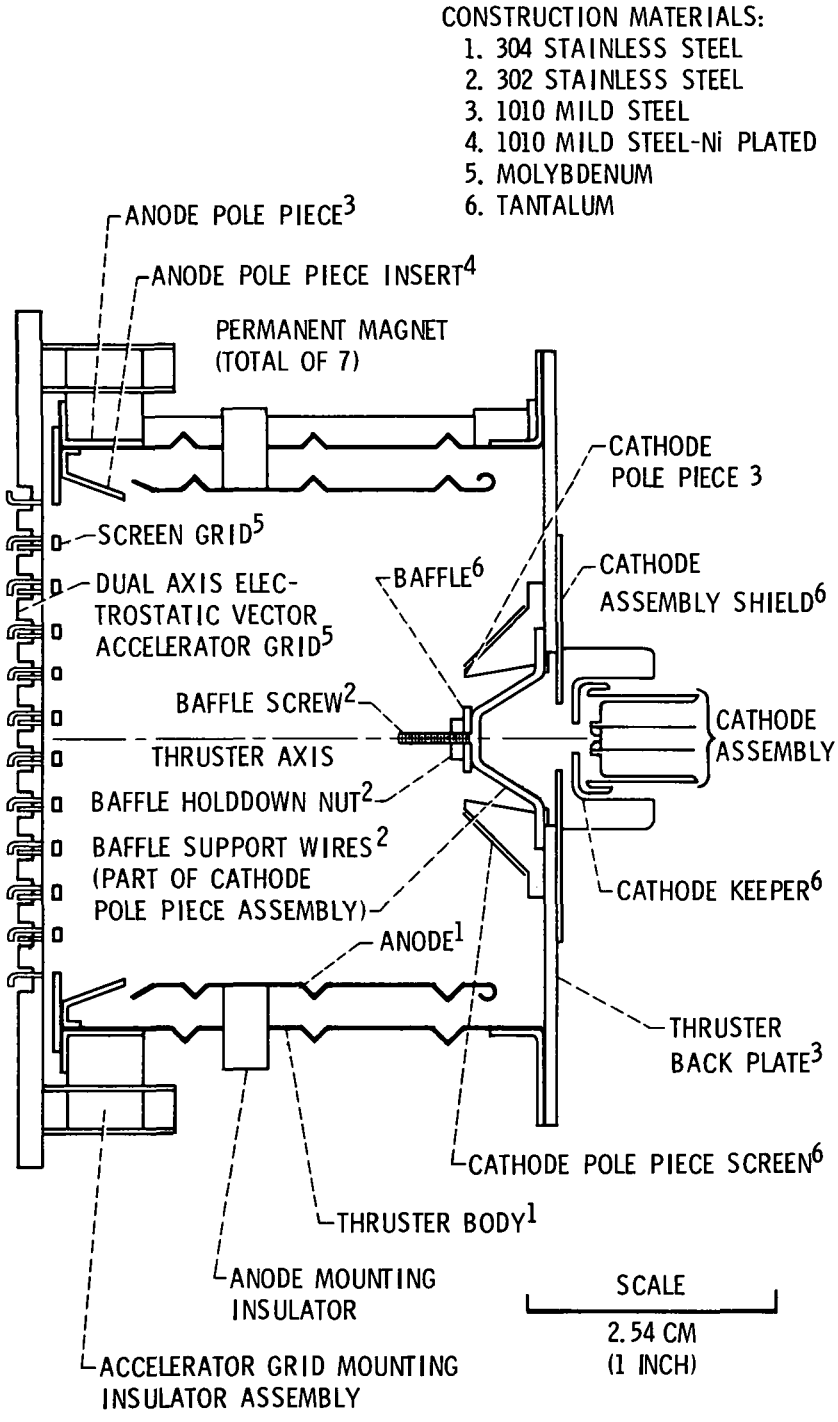

Figure 1. - 5 Centimeter thruster sectional view. (Neutralizer and ground screen not shown.)

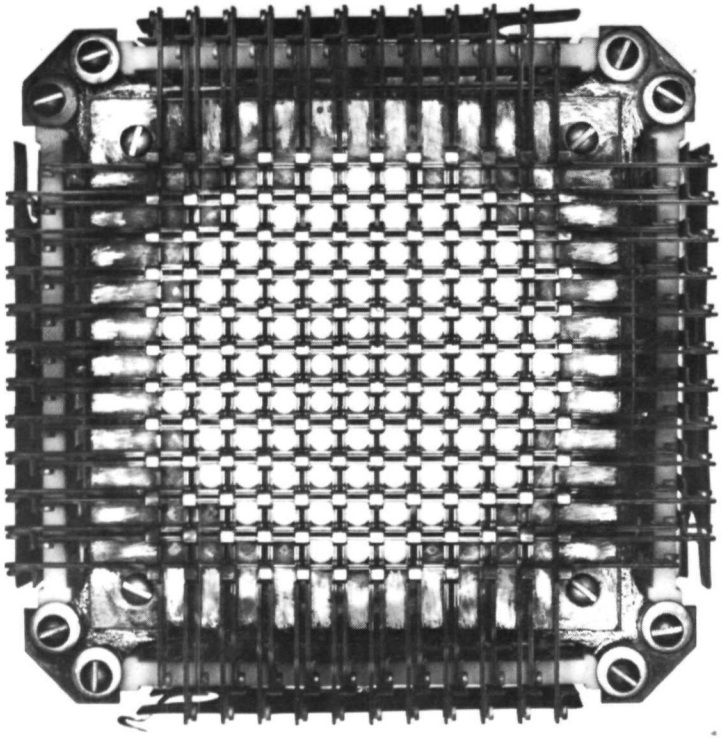

Figure 2. - Hughes electrostatic vector grid system - accelerator side; after final ΔV_I test.

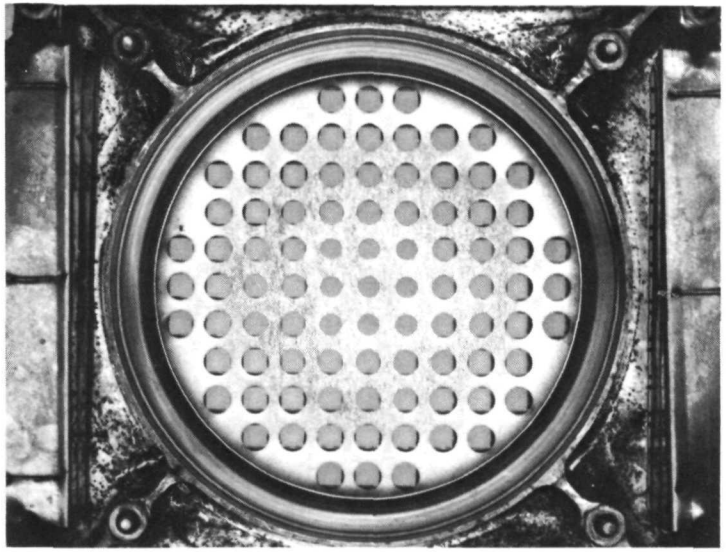

(A) ANODE POLE PIECE INSERT INSTALLED.

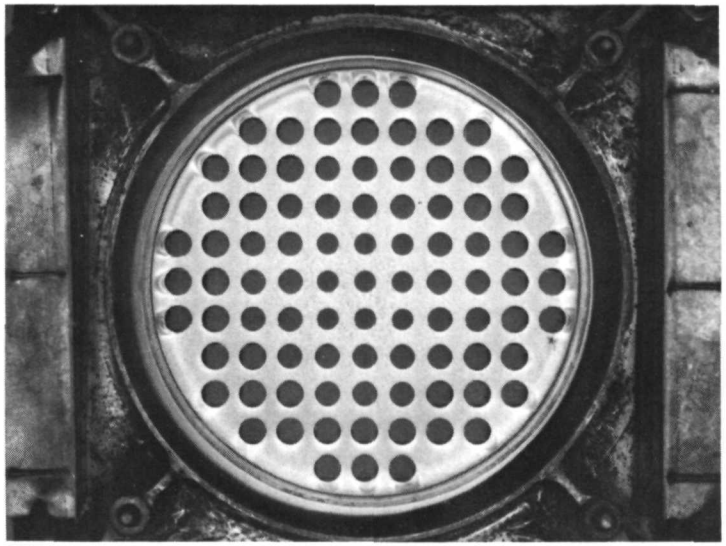

(B) ANODE POLE PIECE INSERT REMOVED.

Figure 3. - Hughes electrostatic vector grid system - screen grid side, after final ΔV_I test.

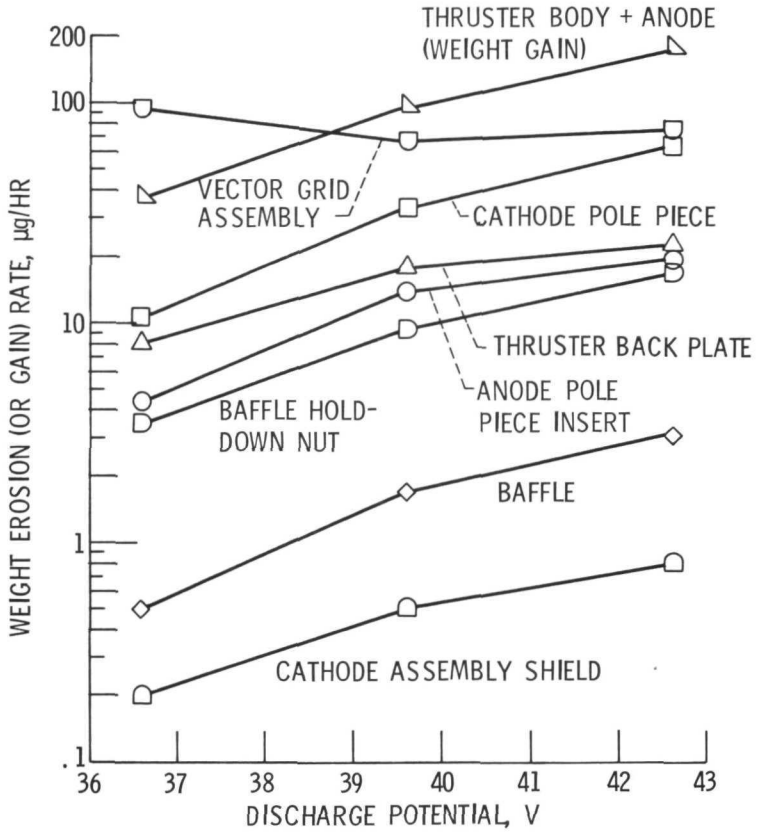

Figure 4. - Weight erosion (or gain) rate of discharge chamber components vs discharge potential.

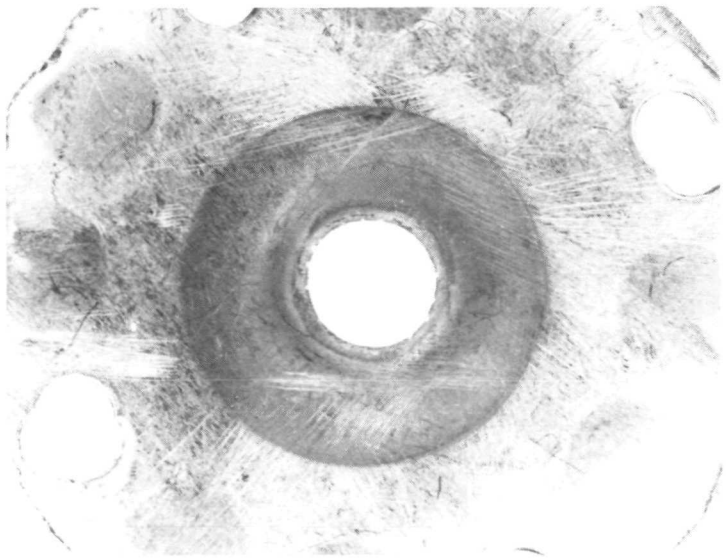

Figure 5. - Cathode assembly shield - downstream side, after ΔV_I = 36.6 V test.

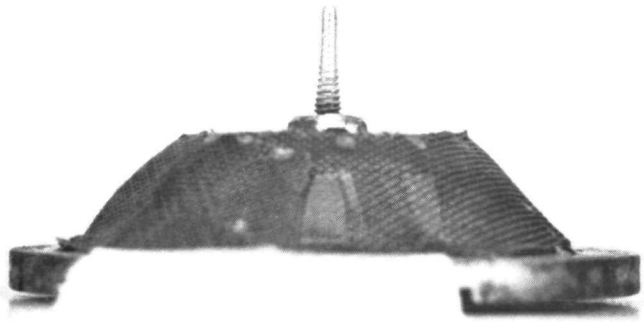

(A) BEFORE FIRST ΔV_I TEST.

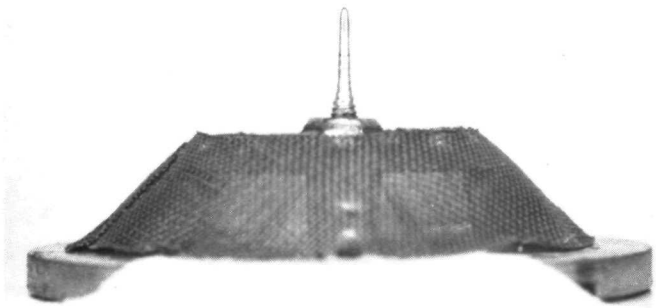

(B) AFTER FINAL ΔV_I TEST.

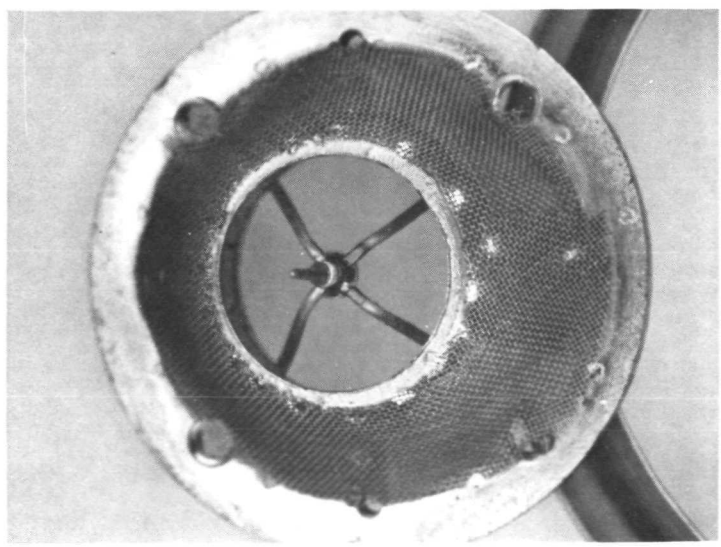

(C) DOWNSTREAM SIDE, AFTER FINAL ΔV_I TEST.

Figure 6. Cathode pole piece with baffle and baffle nut assembled.

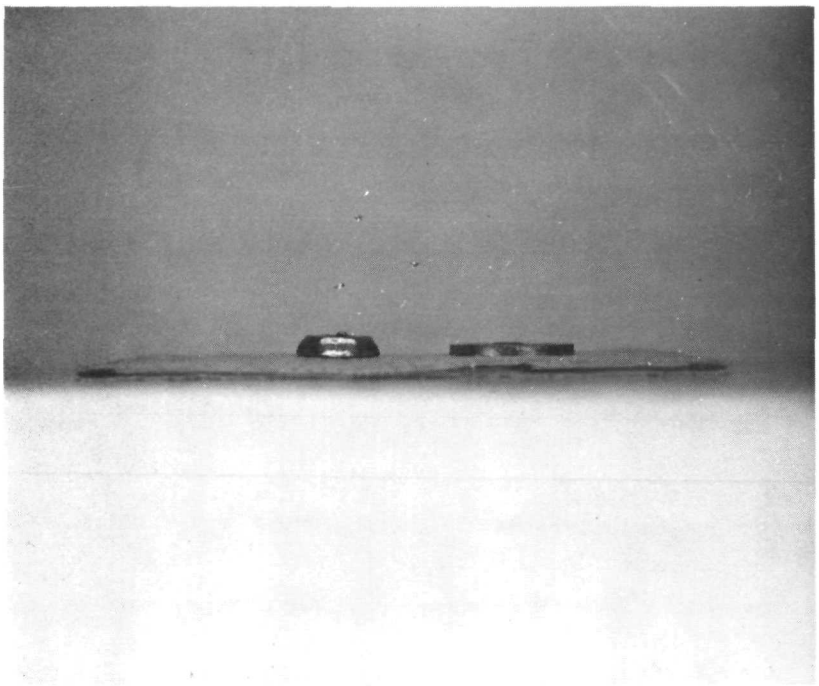

Figure 7. - Baffle and baffle hold-down nut - downstream sides up; after final ΔV_I test.

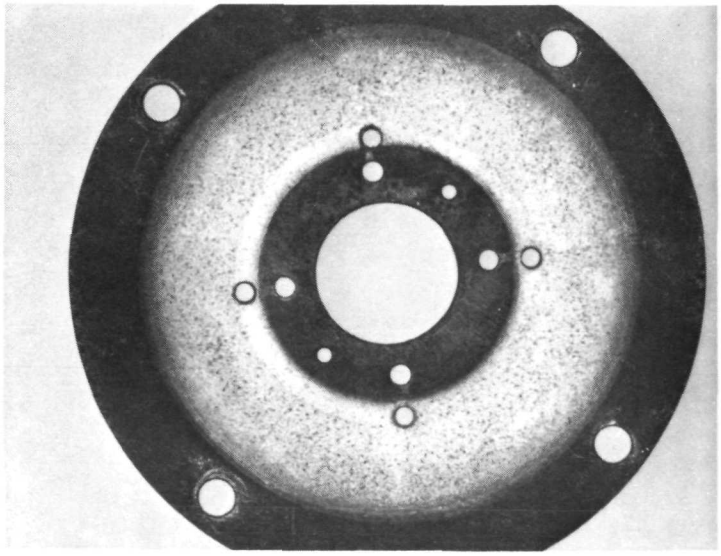

Figure 8. - Downstream side of thruster back plate after ΔV_I = 39.6 V test.

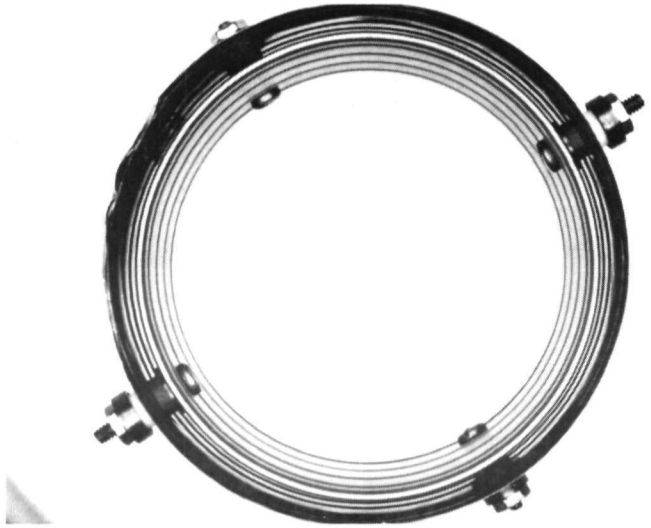

(A) LOOKING DOWNSTREAM.

(B) UPSTREAM END.

Figure 9. - Anode assembly of thruster body after final ΔV_I test.

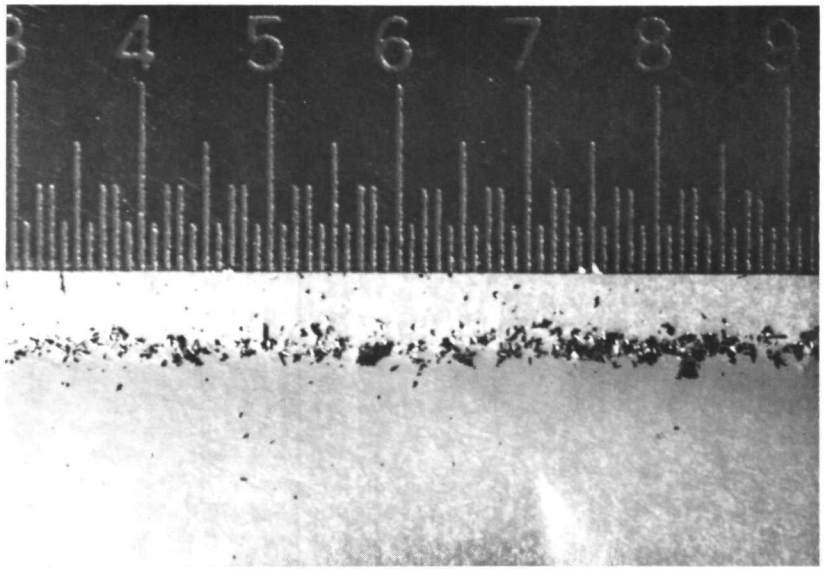

Figure 10. - Magnified view of metal chips collected from thruster body interior after final ΔV_I test. Smallest ruler intervals are hundredths of an inch.

Figure 11. - Anode pole piece insert viewed from downstream side, after final ΔV_I test.

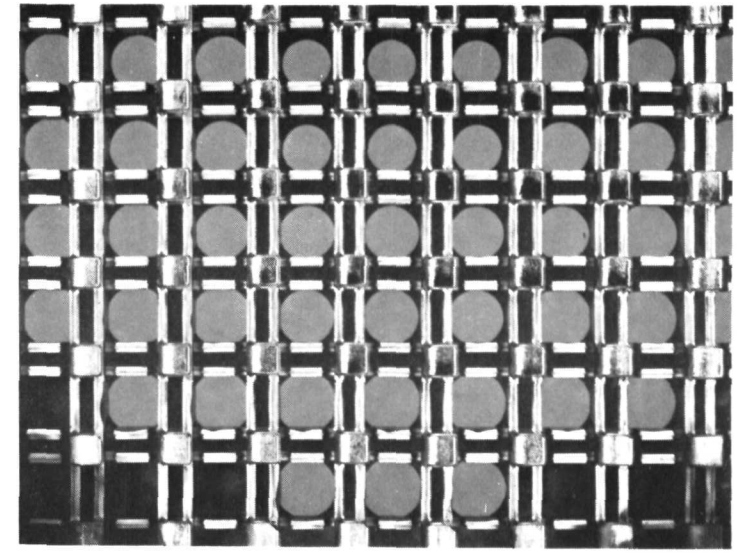

(A) BEFORE FIRST ΔV_I TEST.

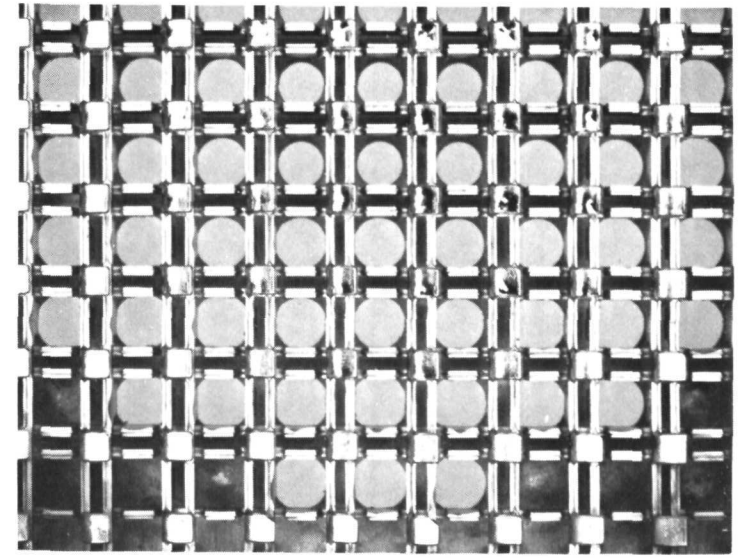

(B) AFTER FINAL ΔV_I TEST.

Figure 12. - Accelerator grid section nearest the neutralizer.

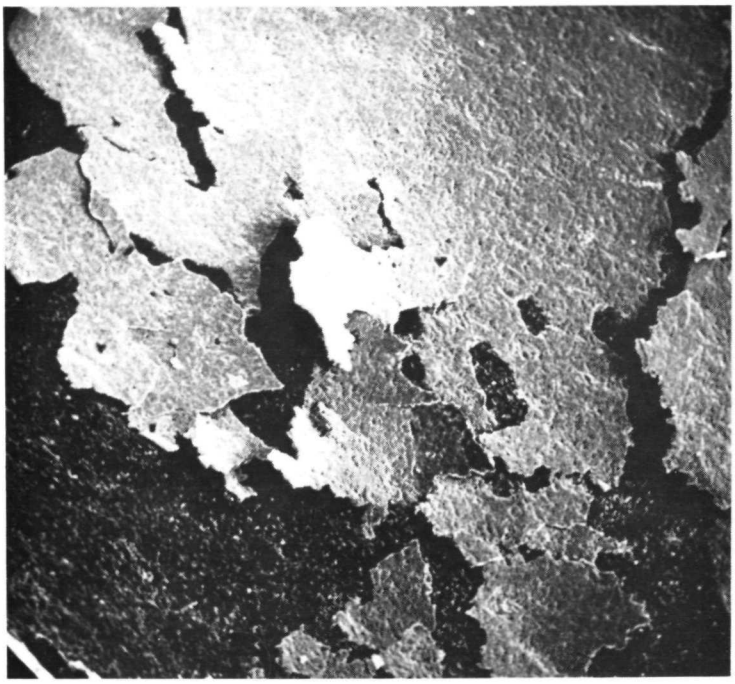

(A) DOWNSTREAM END OF ANODE; X100.

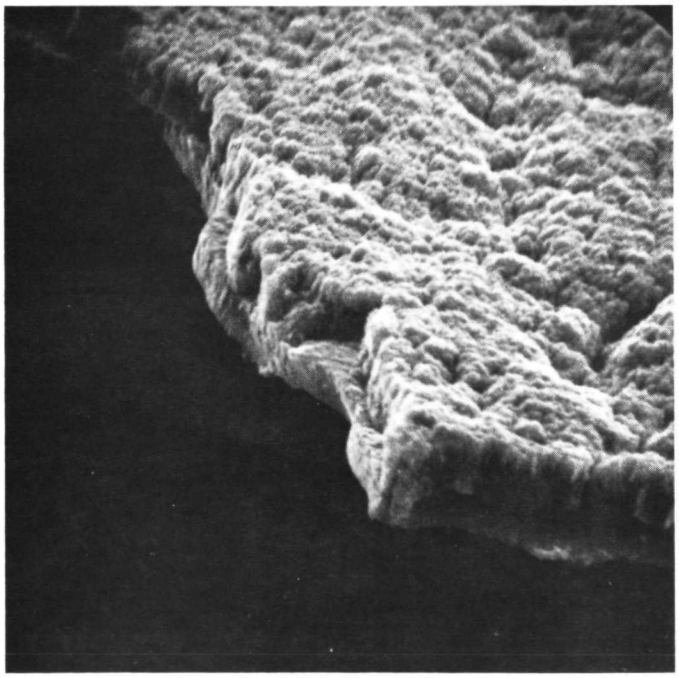

(B) FLAKE EDGE; X3000.

Figure 13. - Number 1 anode coating sample; ΔV_I tests.

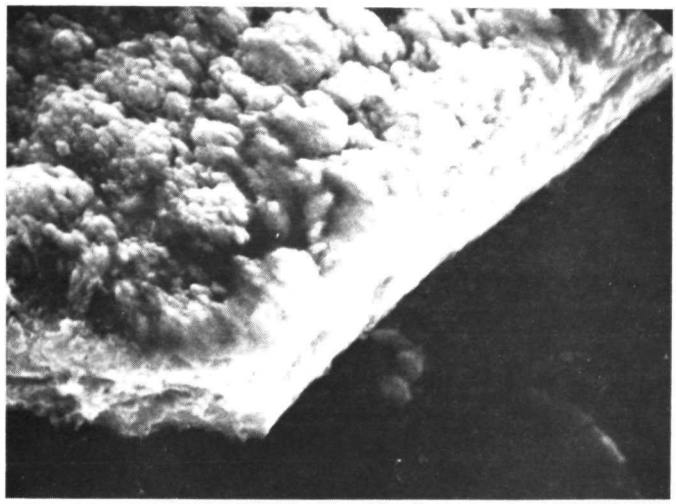

(A) NUMBER 1 ANODE COATING SAMPLE.

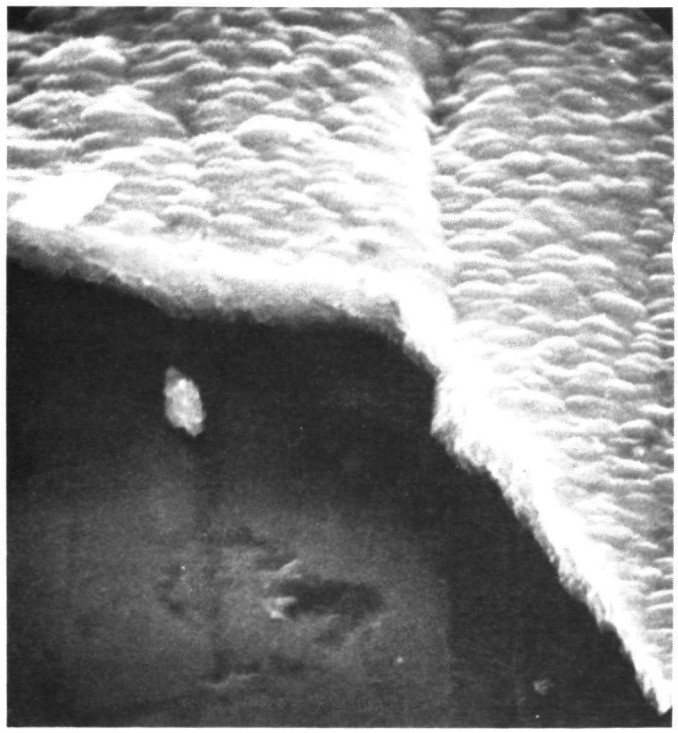

(B) NUMBER 2 ANODE COATING SAMPLE.

Figure 14. - Flake edges; ΔV_I tests; X10 000.

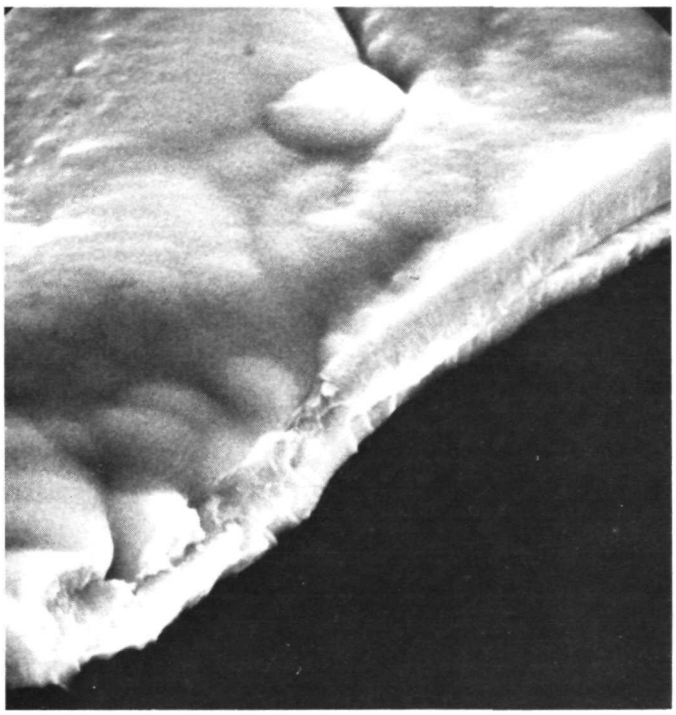

(C) NUMBER 3 ANODE COATING SAMPLE.

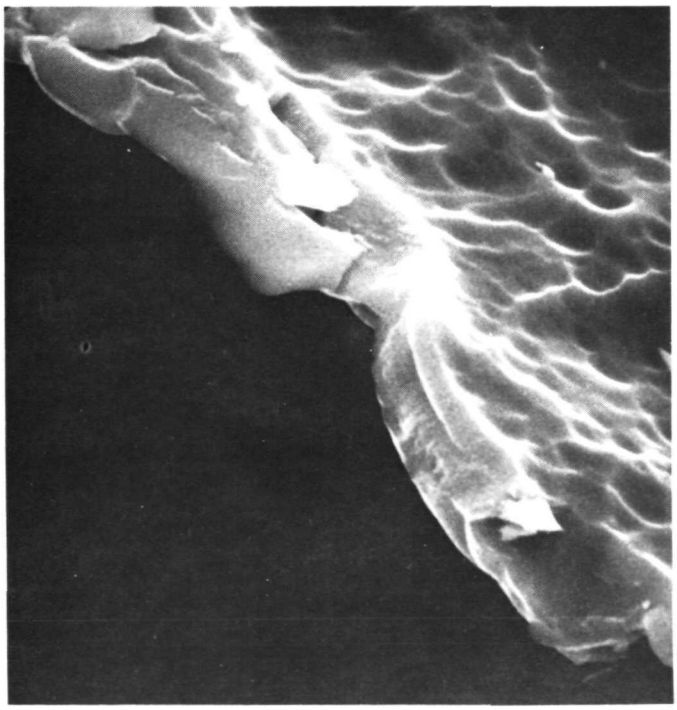

(D) NUMBER 4 ANODE COATING SAMPLE.

Figure 14. - Continued.

(E) NUMBER 5 ANODE COATING SAMPLE.

Figure 14. - Concluded.

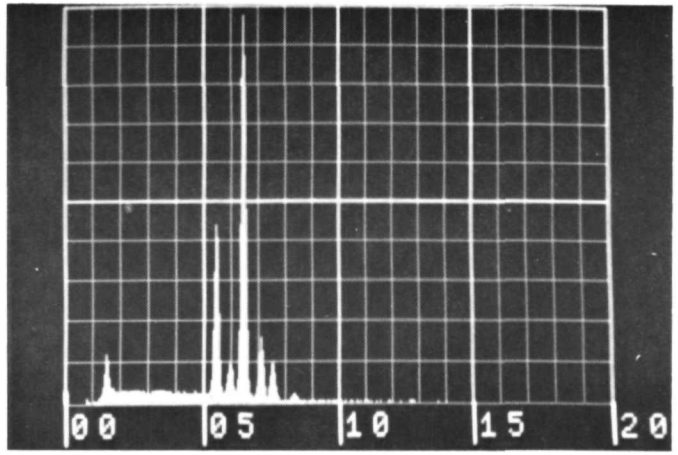

(A) UNUSED TYPE 304 STAINLESS STEEL.

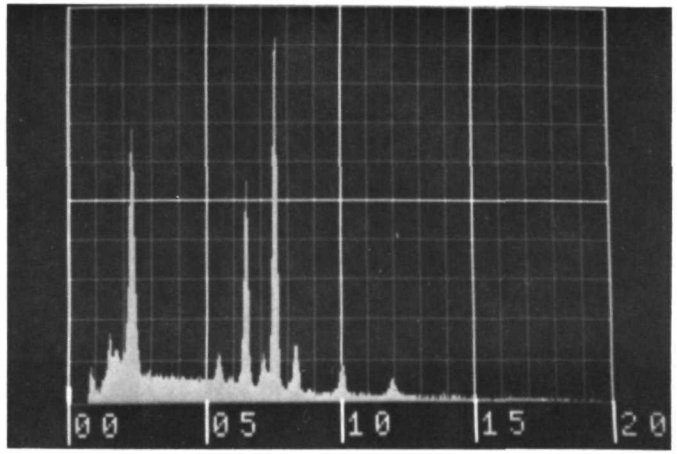

(B) NUMBER 1 ANODE COATING SAMPLE, COATING SURFACE; ΔV_I TESTS.

Figure 15. - SEM X-ray analysis spectrums, counts per channel plotted vs. x-ray energy in keV.

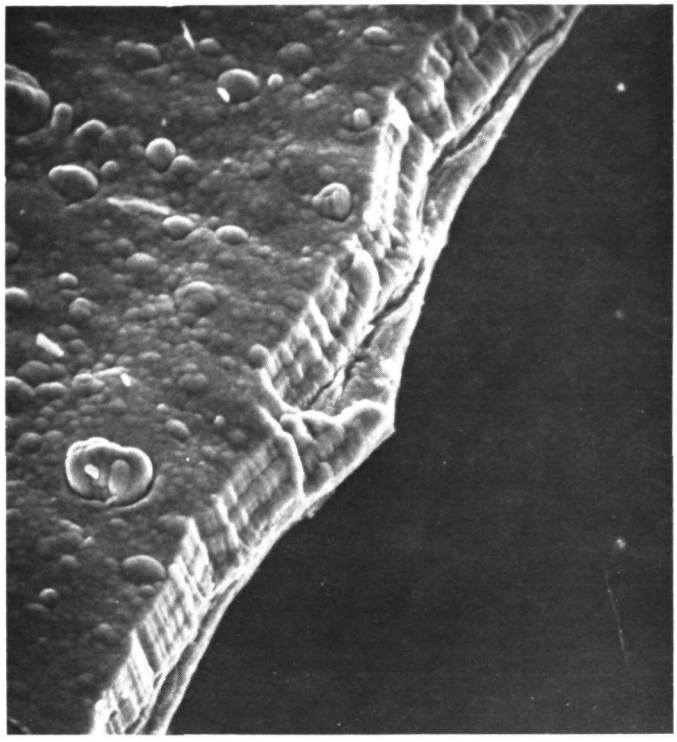

(A) EDGE VIEW.

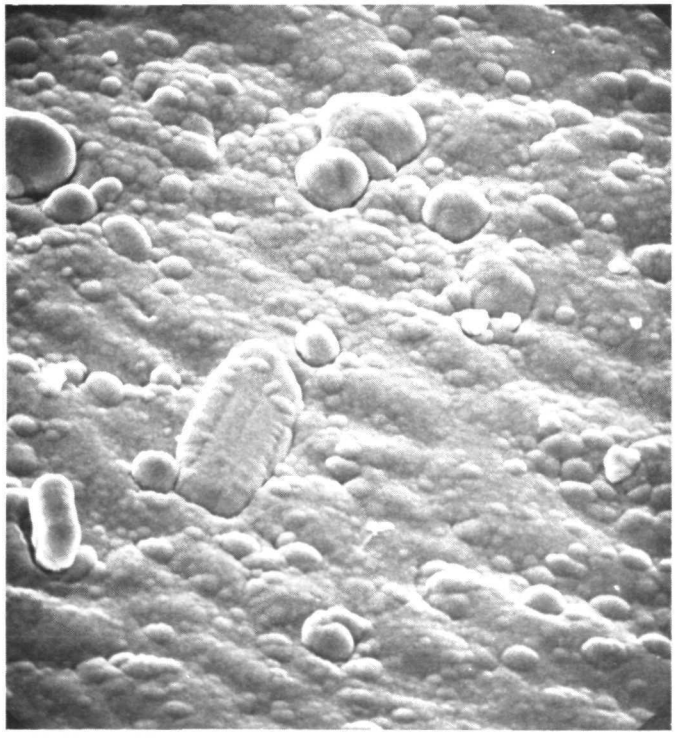

(B) SURFACE VIEW.

Figure 16. - Upstream anode coating flake mounted top side up; from endurance test. X1000.

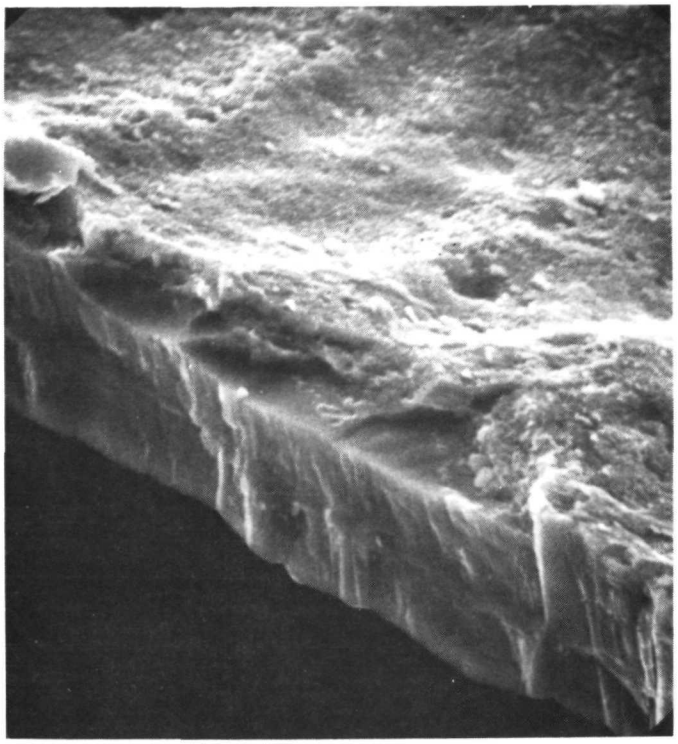

(A) X3000.

(B) X1000.

Figure 17. - Upstream anode coating flake mounted under side up; from endurance test.

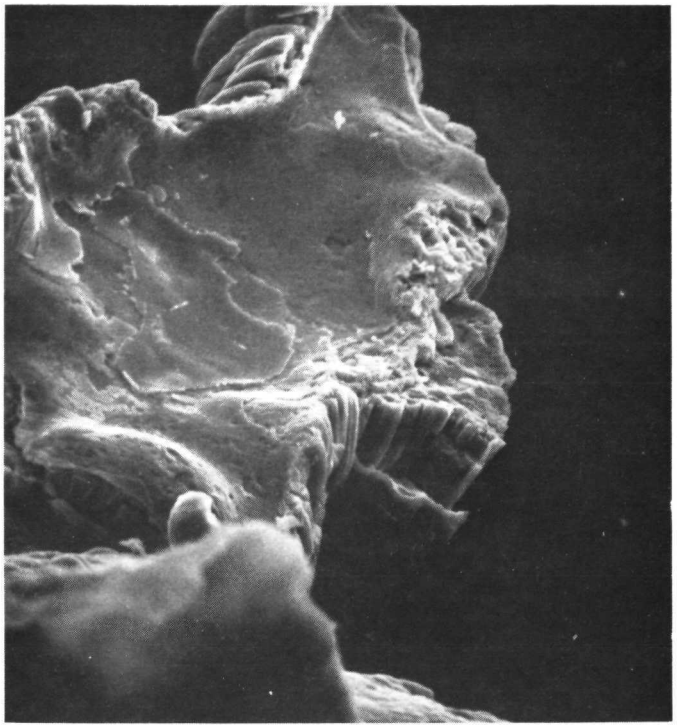

(A) FLAKE MOUNTED UNDER SIDE UP.

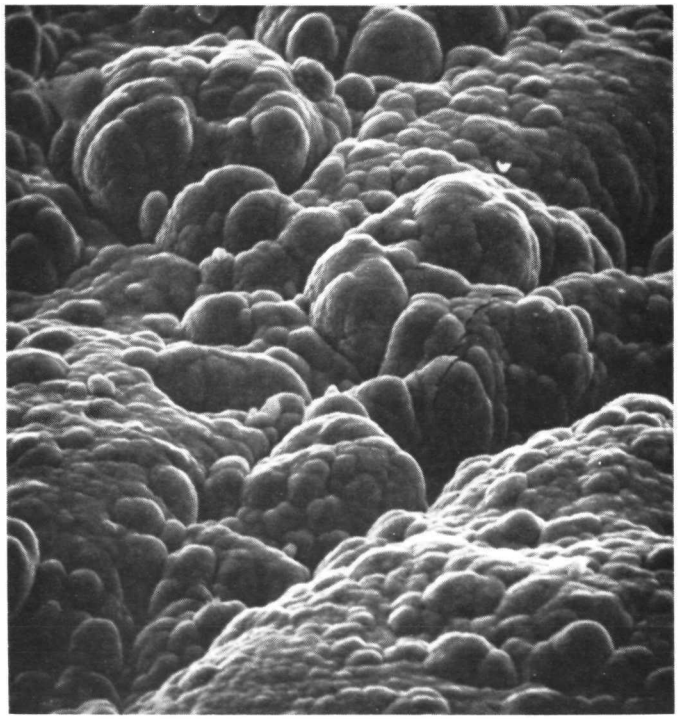

(B) FLAKE MOUNTED TOP SIDE UP.

Figure 18. - Downstream anode coating flake from endurance test. X1000.

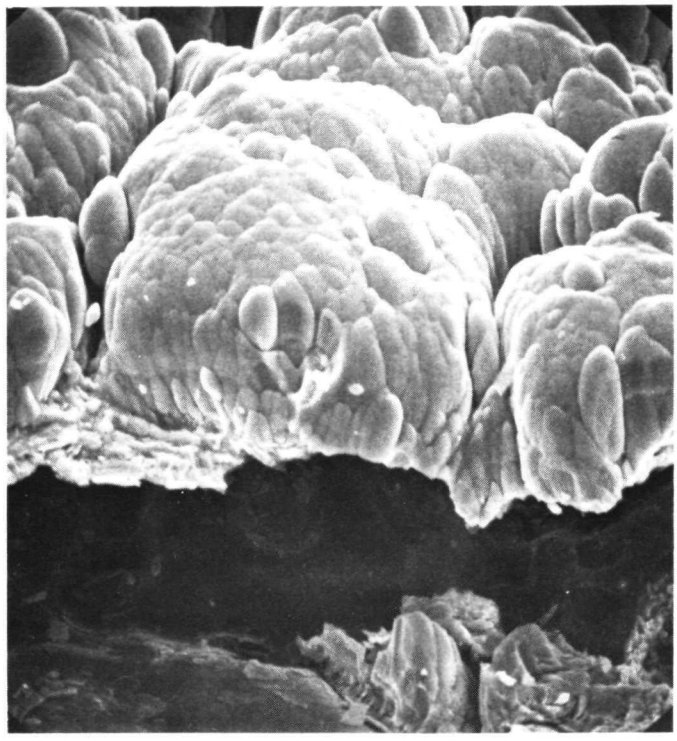

(C) FLAKE EDGE.

Figure 18. - Concluded.

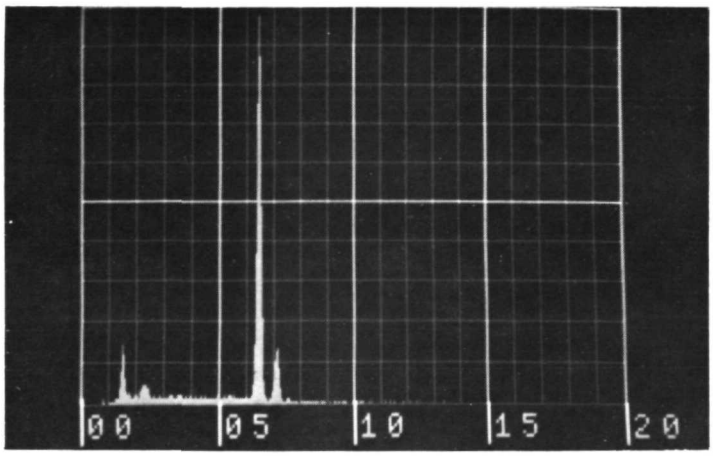

(A) TOP SURFACE OF COATING FLAKE.

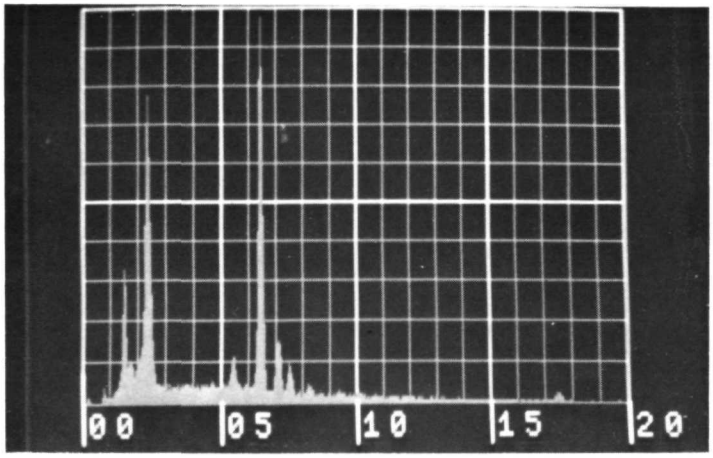

(B) COATING SURFACE.

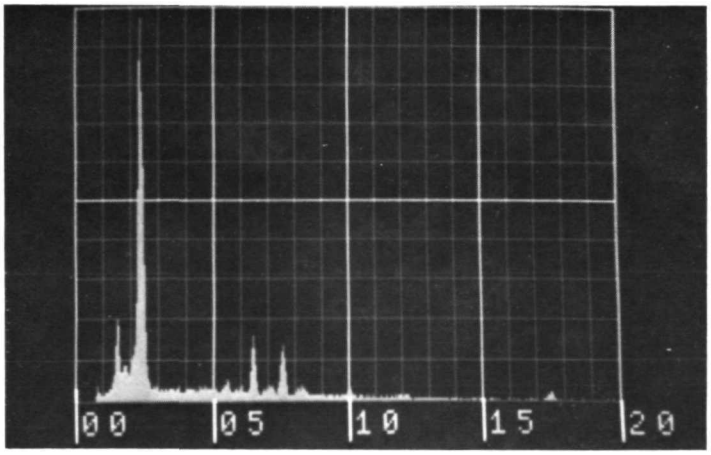

(C) UNDER SURFACE OF COATING FLAKE.

Figure 19. - SEM X-ray analysis spectrums on downstream anode coating, from endurance test.

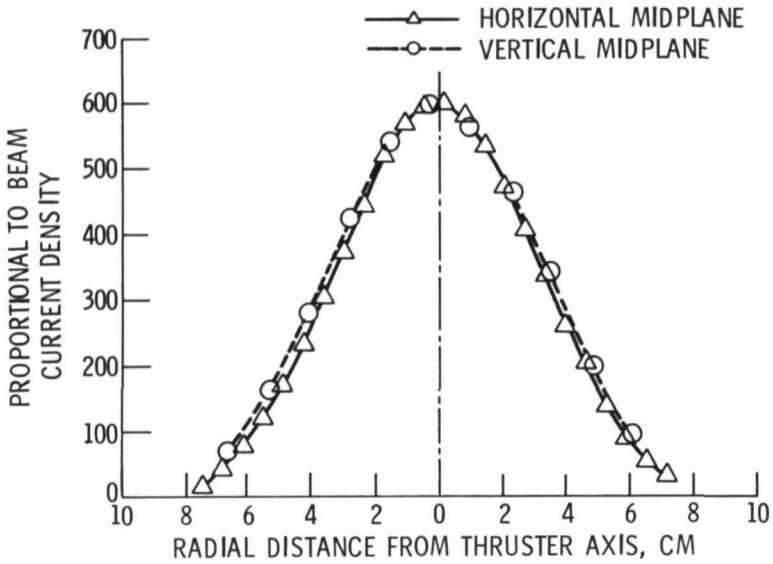

Figure 20. - 5 cm Thruster beam profile 12 cm from grids. ΔV_I = 39.6 V.

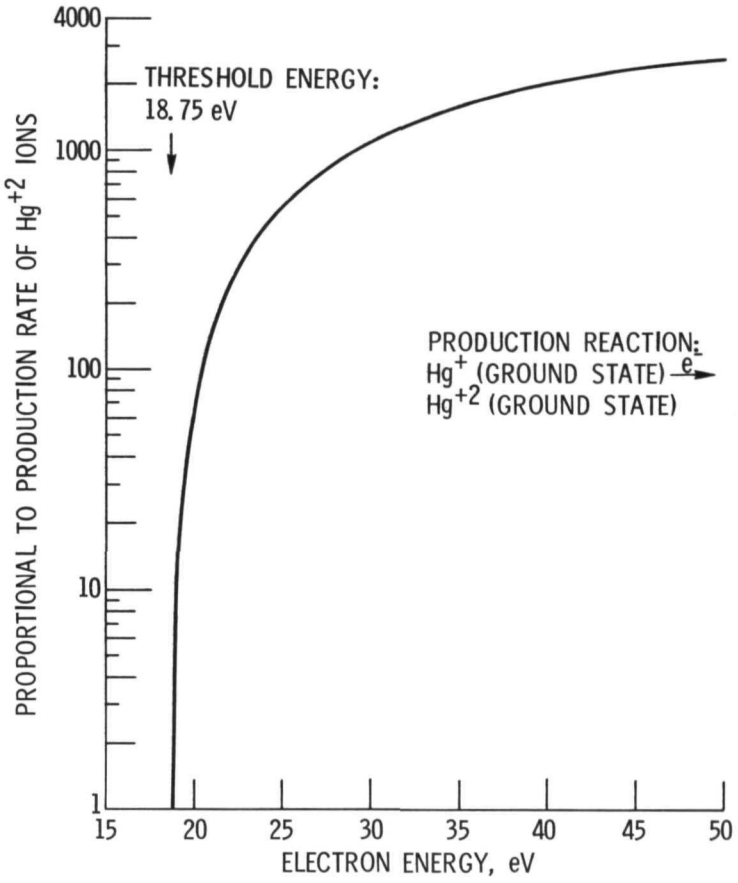

Figure 21. - Theoretical production rate of Hg^{+2} ions; dependence on primary electron energy.

NASA-Lewis